Investigation of hexagonal 2D super structures by dynamic force spectroscopy

-Boron nitride and graphene on transition metals-

Inauguraldissertation

zur

Erlangung der Würde eines Doktors der Philosophie
vorgelegt der
Philosophisch-Naturwissenschaftlichen Fakultät
der Universität Basel

von

Dipl. Phys. Sascha Koch

geboren in Glandorf (Niedersachsen), Deutschland

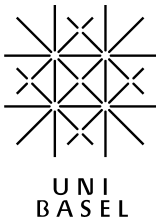

Basel, 2012

Genehmigt von der Philosophisch-Naturwissenschaftlichen Fakultät

auf Antrag von

Prof. Dr. Ernst Meyer, Prof. Dr. Martino Poggio

Basel, den 13. Dezember 2011

Prof. Dr. Martin Spiess, Dekan

creative commons

Namensnennung-Keine kommerzielle Nutzung-Keine Bearbeitung 2.5 Schweiz

---

Sie dürfen:

das Werk vervielfältigen, verbreiten und öffentlich zugänglich machen

Zu den folgenden Bedingungen:

Namensnennung. Sie müssen den Namen des Autors/Rechteinhabers in der von ihm festgelegten Weise nennen (wodurch aber nicht der Eindruck entstehen darf, Sie oder die Nutzung des Werkes durch Sie würden entlohnt).

Keine kommerzielle Nutzung. Dieses Werk darf nicht für kommerzielle Zwecke verwendet werden.

Keine Bearbeitung. Dieses Werk darf nicht bearbeitet oder in anderer Weise verändert werden.

- Im Falle einer Verbreitung müssen Sie anderen die Lizenzbedingungen, unter welche dieses Werk fällt, mitteilen. Am Einfachsten ist es, einen Link auf diese Seite einzubinden.
- Jede der vorgenannten Bedingungen kann aufgehoben werden, sofern Sie die Einwilligung des Rechteinhabers dazu erhalten.
- Diese Lizenz lässt die Urheberpersönlichkeitsrechte unberührt.

Quelle: http://creativecommons.org/licenses/by-nc-nd/2.5/ch/ Datum: 3.4.2009

„Wissenschaft ist keine Frage der Nützlichkeit, sondern des Fortschritts!"
Vicco von Bülow (Loriot)

Abstract

The 2D hexagonal superstructures of *h*-BN on Rh(111) and graphene on Ru(0001) were prepared. By Dynamic Force Microscopy(DFM) as well as spectroscopy methods, these superstructures, which are due to specific lattice mismatches between the overlayer and atomic lattice were highly resoluted partly using bimodal DFM and verifying former investigations done by scanning tunneling microscopy and photo electron spectroscopy. On both samples, a contrast inversion of the superstructure was observed, so that the former elevations appeared depressed. Further, 2D force spectroscopy maps for the first time pointed out that a probably elastic deformation of the elevated sites of the superstructure is the reason for the observed contrast switching. Additionally, Kelvin Probe Force Microscopy measurements (KPFM) were complemented by 2D KPFM maps. The results showed, that the substrate bonded sites of the 2D monolayers are areas of lower work function, which is supported by former PES measurements as well as calculations. Finally the influence of a elastic deformation or rather contrast inversion on the workfunction was determined, showing an increasing of work function for the elevated sites pushed towards the transition metal substrate.

Contents

Chapter 1

Motivation and Outline

Since the first fire was controlled by the mankind, a lot of periods have passed, and inventions and discoveries were made. The industrialization came up by the power of steam and steel. New technologies arised using the new discovered semi-metallic behaviour. Transistors and computers, as we know them today, were invented leading to a second industrial revolution towards a connected world and even influenced and changed our everyday social life. The next step might already be done by opening the door towards the small nano world by the great invention of a new type of microscopes by Binnig, Rohrer, Quate, and Gerber probably leading to the next technological revolution [1, 2]. The manipulation of xenon atoms on a nickel surface by Eigler *et al.* showed that the manipulation of single atoms on the nanometer scale is possible [3]. The detection and investigation of forces and energies on surfaces between molecules or atoms was now also enabled and leading to the imaging and visualization of the exact internal structure of a single pentacene molecule by Gross *et al.* [4]. With these probing methods, also materials of lower dimensions could be observed for the first time in history. The most famous representative graphene, a two-dimensional hexagonal carbon layer, is of highest interest for nowadays science and engineering. Its lower dimensionality changes its physical behaviour and material properties [5, 6, 7] compared to its three dimensional counterpart, graphite. New ways of device engineering are opened as for electromechanical resonators [8], near-field terrahertz probes and detectors [9] or graphene-based capacitors [10]. Embedded in another 2D hexagonal layered material, the hexagonal boron nitride, graphene quantum dots

were investigated [11]. The hexagonal boron nitride (h-BN), a carbon-like structure of boron and nitrogen, is an insulating material, which has almost the same lattice structure compared to graphene. Apart from its electronical properties, it is equally temperature stable as graphene and also has a high heat conductivity. Due to this behaviour it is also named as the "white graphene". This material, grown for example on rhodium (111), is a promissing basic material for the functionalization of surfaces as well as regular arrangement of special atomic clusters [12, 13] and molecules [14, 15]. The investigation of this highly interesting hexagonal 2D materials, which are forming superstructures on transition metals, by the use of *Dynamic Force Microscopy* (DFM) as well as *Spectroscopy* (DFS) is the main goal of the work presented in this thesis. Therefore, first of all the different forces acting between a surface and a probing tip are described in the theoretical chapter 2. Their detection by the use of an *Atomic Force Microscope* (AFM) at room temperature is then elucidated in chapter 3, where fundamental methods as well as newer scanning methods are described. Chapter 4 and 5 are summarizing the experimental setup and the preparation of the probes and samples used. The last two chapters 6 and 7 are presenting the results of the AFM experiments done on superstructures of h-BN on rhodium (111) as well as on graphene on ruthenium (0001) which are verifying former results but also shape a new view on the mechanical behaviour of these materials.

Chapter 2

Forces

From the old greeks Aristoteles and Archimedes to Galileo Galilei and Isaac Newton to the actual modern physics, the history of the understanding of forces and their exact mathematical description is still going on. In the parlance force means in principle that an "influence" on something or someone is causing a change of its actual state. If we are "forcing" someone, we are changing the normal behaviour or nature. In classical physics the changed actual state means a state of motion. Galileo Galilei showed experimentally, that all particles or bodies are keeping their state of motion until a force is changing their direction and/or velocity. Before, it was generally assumed that a force is needed for a constant body movement. This simple assumption was a result of an everyday observation: a moving body becomes slower without a pushing force. Of course, this description is completely ignoring the braking forces like friction (see Fig. 2.1), which is slowing down a moving object if the friction is bigger than the accelerating force or is exactly compensating the acceleration resulting in a constant velocity of the moving object. In "*Philosophiæ Naturalis Principia Mathematica*" Isaac Newton ("forced" by an apple) took Galileo's idea and defined the force as being proportional to the change of a mass' velocity in time (acceleration) or in short: $\vec{F} = m \cdot \vec{a}$, where $\vec{F}$ is the force vector, $\frac{d\vec{v}}{dt} = \vec{a}$ the change of the velocity vector in time and m the mass of the moving body. Nowadays, our knowledge is expanded to a model of four fundamental interaction forces which are: gravitational-, weak-, electromagnetic- and strong interaction. However, in this work and the following chapters and sections it will be focused only on the electromagnetic interaction forces which are

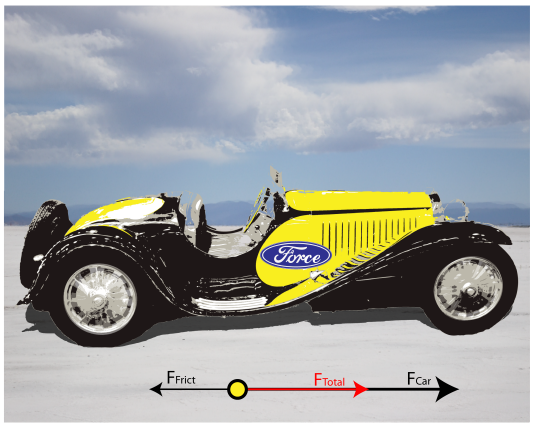

Figure 2.1: Illustration of a moving car. In order to move a car with a constant acceleration, the force $\vec{F}_{Car}$ has to be be bigger than the opposing frictional force $\vec{F}_{Frict}$ which is caused for example by the interaction of the wheels with the ground as well as by the opposing wind. Is the absolute value of $\vec{F}_{Car}$ smaller than the absolute value of the friction force $\vec{F}_{Frict}$, the car will be braked, or will not change its velocity if $F_{Car} = F_{Frict}$. So, the total force can be described by: $\vec{F}_{Total} = \vec{F}_{Car} + \vec{F}_{Frict}$.

containing the short range chemical forces as well as the long range VAN DER WAALS- and electrostatic forces. Although the magnetic forces are included in the eletromagnetic interaction they are not part of this work and will not be discussed further.

2.1 van der Waals Forces

The idealization of physical systems was always a standard procedure for simplifying the mathematical description of experimental observations. A good example is the ideal gas equation:

$$pV = RT, \tag{2.1}$$

where p is the pressure caused by the ideal gas in the volume V with the temperature T. $R = Nk_B$ is the gas constant with k_B as the BOLTZMANN constant. The ideal gas equation is based on the predictions of ROBERT BOYLE, EDMÉ MARIOTTE as well as JOSEPH GAY-LUSSAC. Although this gas law is still in use and gives mostly a good approximation of the relation of pressure, volume and temperature it is not reflecting the reality. It is

Figure 2.2: A Gecko showing his attraction to surfaces [16].

ignoring the fact, that all atoms and molecules in a gas are in interaction with each other and can not explain the effect of adhesion and cohesion. Sir J.E. Lennard-Jones described it ones like this: "*There are in nature, as in politics, two opposing forces. One of these aims at a peaceful consolidation and the other at a more active and probably more spectacular disruptive process. In nature it is cohesion between atoms which tends to produce condensation and solidification, and temperature which tends to produce dissociation...Temperature is a manifestation of kinetic energy and cohesion of potential energy...*" [17]. So there are forces, which are causing an attraction of atoms, molecules or particles. In 1873 the dutch scientist Johannes Diderik van der Waals presented a way to describe this fundamental property of matter by:

$$(p + \frac{a}{V^2})(V - b) = RT. \tag{2.2}$$

In comparison to the ideal gas law (eq.2.1) the van der Waals equation of state (eq. 2.2) contains two important innovations : the term $(V - b)$ is taking into account the finite size of the elements in the real gas b by its substraction from the volume V and $\frac{a}{V^2}$ is an element specific additive to the pressure due to the attractive intermolecular or interatomic force: the

van der Waals force (vdW force) [18]. If $a = b = 0$, equation 2.2 becomes equal to the ideal gas equation. The attractive vdW force is for example responsible for the non-covalent binding between atoms and molecules like in water or is also the reason why a gecko can walk overhead (see Fig. 2.2). But how can the vdW force be described? van der Waals forces have their origin in dipole-dipole interactions or better by dipole fluctuations or induced dipoles by changed electric fields. For a mathematical description, a small approach has to be done using the experience of the past concerning the form of known potentials like gravitation or Coulomb interaction. Both are potentials of the form:

$$\Phi(r) = -\frac{C}{r^n}, \tag{2.3}$$

where r is the distance between two objects (planets, charges, etc.), C a constant which is characteristical for the observed objects and the exponent n coresponds to the strength of the interaction (e.g. n=1 for the gravitation). In relation to this, the vdW interaction energy between two atoms was found to be [18]:

$$\Phi_{vdW}(r) = -\frac{C}{r^6}. \tag{2.4}$$

Due to the work of Fritz Wolfgang London and Michael Polanyi the potential of a single atom at a distance r to the flat surface [19, 18] is expressed by:

$$\Phi_{vdW}(r) = -\frac{\rho\pi C}{6r^3}. \tag{2.5}$$

In this equation the density of atoms in the surface ρ is included as well as their vdW interaction. For a more macroscopic system like a sphere above the same flat surface, the equation 2.5 has to be integrated over the distance r between the atomic layers of the sphere and the flat surface. Fig. 2.3 [18] is a graphic illustrating a sphere above a flat surface. For the calculation of the vdW potential and force it is useful to find a infinitesimal volume. Here the sphere is divided into circular sections with an surface of $\pi x^2 = \pi(2R-r)$ and a height of dr. In this way a total number of atoms in the sphere with a distance (D+r) from the surface is $\rho\pi(2R-r)rdr$. By the use of eq. 2.5, it can be integrated as follows:

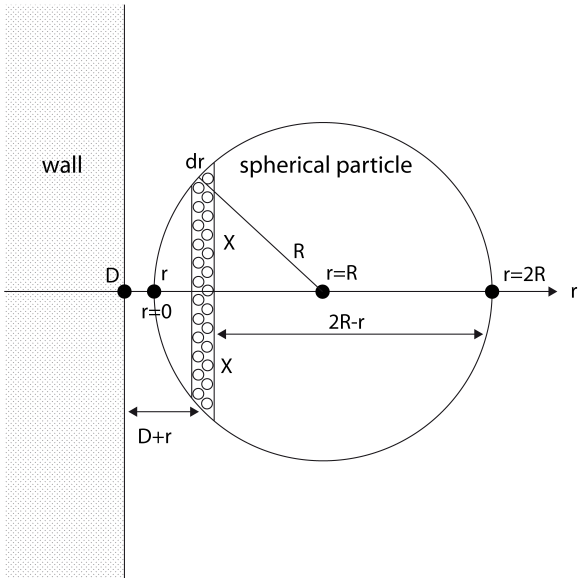

Figure 2.3: Illustration of the integration method for a sphere close to a wall/surface like it is done by J.N. Israelachvili [18].

$$\Phi_{vdW}(r) = -\frac{\rho^2\pi^2 C}{6}\int_0^{2R}\frac{(2R-r)r}{(D+r)^3}dr. \tag{2.6}$$

Assuming that $D << R$ and $z \approx D$, with the substitution $p = D + r$ we get:

$$\Phi_{vdW}(r) = -\frac{\rho^2\pi^2 C}{6}\int_0^{\infty}\frac{(2R)r}{(D+r)^3}dr \Rightarrow \Phi(p) = \frac{2R\rho^2\pi^2 C}{6}\int\frac{(p-D)}{p^3}dp \tag{2.7}$$

$$\Leftrightarrow \Phi_{vdW}(p) = \frac{2R\rho^2\pi^2 C}{6}\left[-\frac{1}{p}\right] + \left[\frac{D}{2p^2}\right]. \tag{2.8}$$

Substituting back to r and with the boundaries ∞ and 0 the vdW potential between the sphere and the flat surface is:

$$\Phi_{vdW}(r) = \frac{2R\rho^2\pi^2 C}{6}\left[-\frac{1}{D+r}\right]_0^{\infty} + \left[\frac{D}{2(D+r)^2}\right]_0^{\infty} \tag{2.9}$$

$$\Leftrightarrow \Phi_{vdW}(D) = \frac{R\rho^2\pi^2 C}{6D}. \tag{2.10}$$

In general the force is defined as:

$$F(r) = -\frac{d\Phi(r)}{dr}, \tag{2.11}$$

which leads to the following expression for the van der Waals force in dependence of the sphere-surface distance D:

$$F_{vdW}(D) = -\frac{R\rho^2\pi^2 C}{6D^2} = -\frac{RA_H}{6D^2}. \tag{2.12}$$

$A_H = \rho_1\rho_2\pi^2 C$ is called the Hamaker constant, named after H.C. HAMAKER. A_H is depending of the material and is normally in the range of $10^{-19}J$ [19, 18]. The computed term for the van der Waals potential and force are only taking into account an attractive force as shown in the plot of figure 2.4. But in reality, by a closer approach to the surface, also repulsive forces have to be considered. Together with the attractive forces, they are responsible for a stable equilibrium of atoms for example in a crystal lattice. Therefore equations 2.11 and 2.12 are only valid for larger distances.

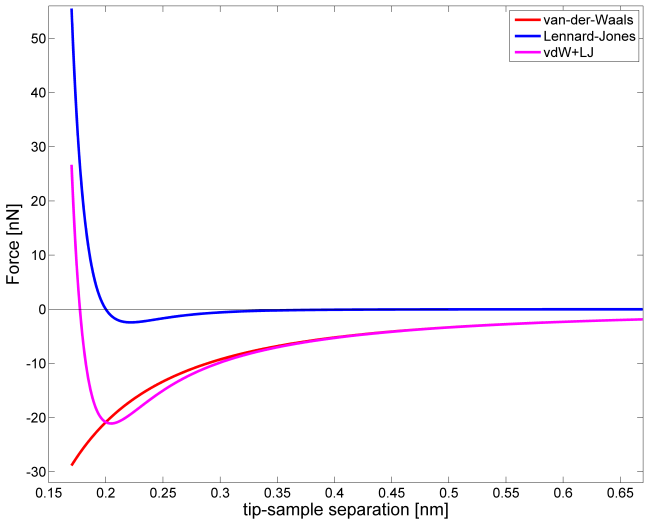

Figure 2.4: Plot of the van der Waals forces, the long- and short range forces expressed by the Lennard-Jones equation as well as the sum of both.

2.2 Chemical Forces

The short range chemical forces can be summarized as the forces acting inter-atomically or -molecularly respectively. This attractive (big atom separation) or repulsive (small atom separation) force is called cohesion. LENNARD-JONES needed an equation for the atomic interaction potential of inert gas (Lennard-Jones potential), which resulted in:

$$\Phi_{LJ}(r) = 4\epsilon \left[\left(\frac{\sigma}{r}\right)^{12} - \left(\frac{\sigma}{r}\right)^{6} \right], \tag{2.13}$$

where $\Phi_{LJ}(r)$ is the attractive or rather repulsive potential between two atoms in dependence of their distance r. σ represents the collision distance of the gas atoms and ϵ is a quantitiy of their attractive energy. These values were determinated in the gas state and the exponents 6 and 12 in equation 2.13 were simply fitting well for the description of the potential between Neon, Argon, Krypton and Xenon atoms: a potential which is attractive at long distances but which becomes repulsive for small ones [20]. Using the definition of the force in eq. 2.11 leads to an expression for the force between two gas atoms due to the interaction potential $\Phi_{LJ}(r)$:

$$F_{LJ}(r) = \frac{24\epsilon}{\sigma} \left[\left(\frac{2\sigma}{r}\right)^{13} - \left(\frac{\sigma}{r}\right)^{7} \right]. \tag{2.14}$$

Adding this term for Lennard-Jones forces to the vdW forces, as mentioned in the last subchapter, the real force behaviour of atoms brought together is described and results in the red curve of Fig. 2.4. The partly empiric formula for the atom-atom interaction F_{LJ} is only one possibility for a mathematical expression of atomic interaction potentials and forces respectively. For solving the SCHRÖDINGER-equation in the case of the potential of a two-atomic molecule in 1929 PHILIP M. MORSE [21] proposed to use:

$$\Phi_M(r) = D \left(e^{-2a(r-r_0)} - 2e^{-a(r-r_0)} \right), \tag{2.15}$$

with r as the intramolecular or atomic distance, r_0 as the relaxation distance of the molecule-atoms (distance of lowest potential energy), a constant a which is characteristic for the molecule and D as an energy minimum for $r = r_0$ (binding energy).

So in principle MORSE chose this formula because it fullfilled 4 requirements [20] for the experimentally observed behaviour of multi atomic systems:

1. Asymptotical convergence to a "finite value" for $r \to \infty$
2. Only one minimum at $r = r_0$
3. Becoming ∞ at $r = 0$
4. Being in accordance to allowed energy levels of the system.

By the use of equation 2.11 an expression for the force can be found:

$$F_M(r) = 2aD\left(e^{-2a(r-r_0)} - e^{-a(r-r_0)}\right). \tag{2.16}$$

If analogue to the expression from LENNARD-JONES the term of equation 2.16 for Morse forces is added to the one for the vdW forces, also the interaction in the short as well as long range regime is described, but in contrast to the Lennard-Jones force, chemical bondings in simple molecules are decribed, as well.

2.3 Electrostatic Forces

Electrostatic forces are caused by charge differences and the resulting potential difference (voltage). The easiest example for such a system is a plate capacitor. But this force is not only a macroscopic effect. It is also important for the interaction between ions or ions and electron charged surfaces. The electrostatic force complies with the coulomb law, named after the french physicist CHARLES AUGUSTIN DE COULOMB. Due to the electric field E_1 of a charge Q_1 at a distance r:

$$E_1(r) = \frac{Q_1}{4\pi\epsilon_0\epsilon_r r^2}. \tag{2.17}$$

COULOMBS' law for the force between two charges Q_1 and Q_2 is defined as:

$$F_C(r) = Q_2 E_1 = \frac{Q_1 Q_2}{4\pi\epsilon_0\epsilon_r r^2}. \tag{2.18}$$

ϵ_0 is the dielectric contant and ϵ_r the material dependend permittivity. For the electric energy due to the electric potential difference $\Delta\Phi_{el}$ between e.g. two capacitor plates and with its capacity $C(z)$ which is in dependence of the distance between the capacitor plates one obtains:

$$W_{el} = \frac{1}{2}C(z)\Delta\Phi_{el}^2. \tag{2.19}$$

Out of this a capacitive force can be defined by:

$$F_{Cap} = -\frac{1}{2}\frac{\partial C(z)}{\partial z}\Delta\Phi_{el}^2. \tag{2.20}$$

This force is acting on every charge $Q = C\Delta\Phi_{el}$ in a capacitive system.

Chapter 3

Atomic Force Microscopy

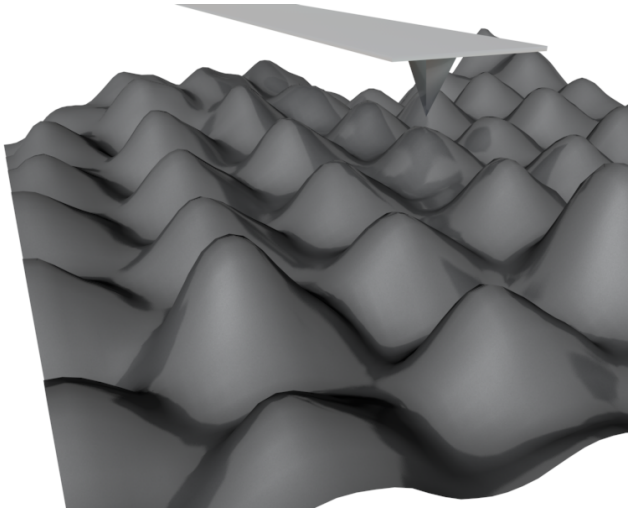

Figure 3.1: AFM tip above a surface.

Since the invention of the Scanning Tunneling Microscope (STM) by Binnig, Rohrer and Gerber [2, 22] observations of surfaces on the nanoscale became possible. Based on the tunneling effect, the STM is limited to conductive and semi-conductive samples by imaging their electronic density of states. This limitation and the need for an easy method to observe forces on the nanoscale (or even less) lead to the invention of the Atomic Force Microscope (AFM) by Binnig, Quate and Gerber [1]. While the first AFM was in principle a STM on a metallic cantilever with a front-end tip, the detection of the cantilever bending due to the forces acting between tip and sample were changed later to an optical readout using a laser and

photodiode detection system (beam deflection AFM)[23]. But also other approaches were made in order to realize an AFM: the tuning fork AFM [24, 25] and the so-called kolibri sensor AFM [26], which both are mainly used to be operated at very low temperatures ($\leq 5\,\mathrm{K}$).
In this section an overview over scanning methods using a beam deflection AFM will be given. Then, in the subsequent chapter "Experimental Setup" the microscope itself will be described more detailed.

3.1 Dynamic Force Microscopy

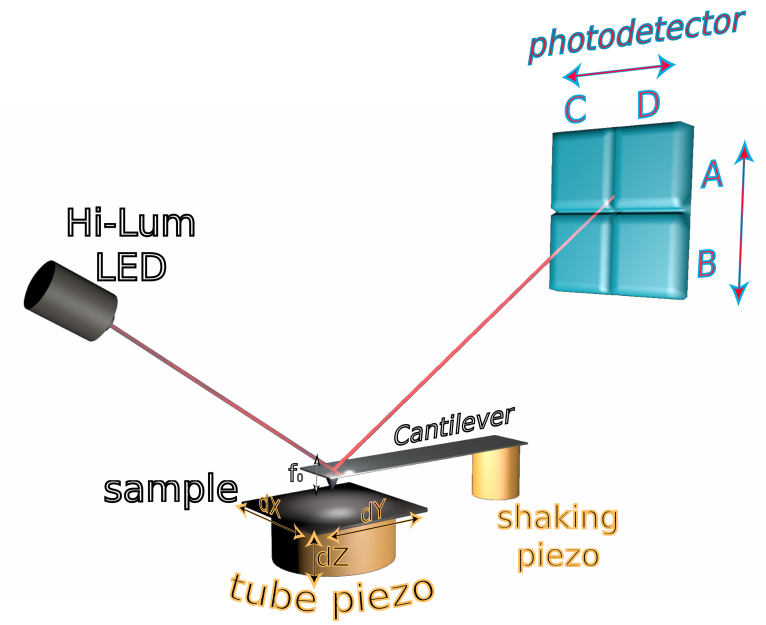

Figure 3.2: Schematic drawing of a beam deflection AFM.

In dynamic force microscopy (DFM) an atomically sharp edged tip at the end of a cantilever bar, mostly made out of silicon, is approached to a sample without contact to the surface (non-contact regime). Therefore, a tip-sample seperation of even less than 0.5 nm can be reached. During this, the cantilever is excited mechanically in resonance by a shaking-piezo using one of the eigenmodes of the cantilever. A detailed view is given in Fig. 3.2 in chapter 4. In basic use, the first eigenfrequency is in the range of $100 - 200\,\mathrm{kHz}$. Using a four quadrant deflection detector and a phase-locked-loop controller (PLL), the amplitude, the phase and the frequency

shift of the oscillation are detected. The changes of these signals are used as error signals for the control of the shaking- and the z-piezo by the PLL feedback, tuning the excitation as well as the tip-sample distance. In general, in the field of the nc-afm or dynamic force microscopy (DFM) methods two modes of operation are used, which are amplitude and frequency modulation, and which will be discussed more detailed in the next two sections.

3.1.1 AM-AFM

In the amplitude modulation mode (AM-AFM), the amplitude of the cantilever oscillation is used as controlling signal [27]. Driven by a constant excitation amplitude A_{exc}, the cantilever is oscillated at a constant frequency f_{exc} which can be chosen slightly higher than its free resonance frequency f_0. By this, far away from the surface, the amplitude of the cantilever behaves under terms of the following equation [27]:

$$A = \frac{A_0(\frac{f_{1st}}{f})}{\sqrt{1+Q^2(\frac{f}{f_{1st}}-\frac{f_{1st}}{f})^2}}. \tag{3.1}$$

f_{1st} is the resonance frequency of the cantilever, f the measured oscillation frequency with $\Delta f + f_{1st} = f$, A_0 the free amplitude at resonance, A the tip vibration amplitude and Q the quality factor of the cantilever. Figure 3.3 illustrates the behaviour of the amplitude vs. frequency shift Δf for different values of Q. When the tip comes closer to the sample surface, the oscillation frequency f is shifting due to the acting forces in the tip-sample system. Consequently, the amplitude A decreases which can be used as an input signal for distance controlling. The shift in the frequency and the reaction in a decreasing amplitude has a time delay $\tau \approx \frac{2Q}{f_{1st}}$, the disadvantage of the AM method. The quality factor Q is a quantity for the signal-to-noise ratio of a cantilever (figure3.3) and a higher Q means a higher sensitivity which is obvious by taking the minimal detectable force gradient into account [28]:

$$\frac{\partial F_{min}}{\partial z} = \frac{1}{A}\sqrt{\frac{2kk_BTB}{2\pi f_{1st}Q}}. \tag{3.2}$$

Here, k is the spring constant and B the bandwith of the detector. As it can be seen, a higher sensitivity, meaning a lower $\frac{\partial F_{min}}{\partial z}$, can be reached by either high resonance frequencies or a high qualtiy factor. Since a high Q

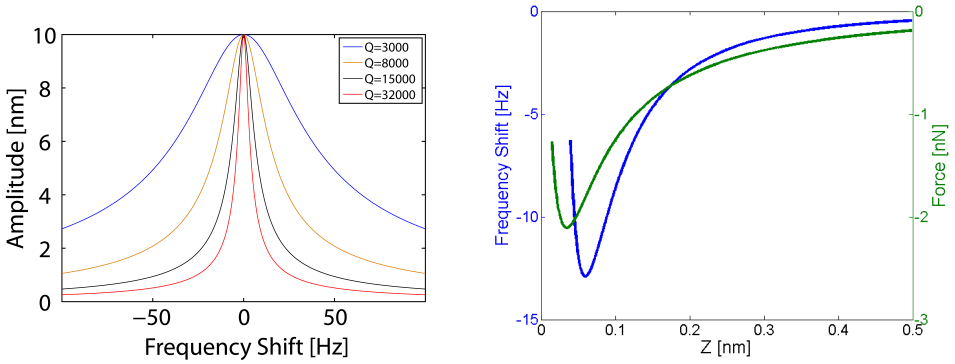

Figure 3.3: Left: Plot of the amplitude versus frequency shift for different quality factors based on equation 3.1. On a shift in the frequency a drop in the amplitude follows. Also, the higher the Q factor the higher the signal and the lower the noise. Right: Plot of the frequencey shift and the force versus the tip-sample distance z.

means also a bigger time delay τ, the controlling system of the amplitude modulation technique, needs always to wait a time constant τ between two measurement points in order to react on the topography signal.

3.1.2 FM-AFM

While the amplitude modulated mode has its drawback in speed, in the frequency modulated atomic force microscopy (FM-AFM) invented by Albrecht *et al.* [28] this is not the case. The FM mode is the true **non-contact mode** because the tip stays always in the attractive regime of the force-distance curve (see Fig. 3.3) above the surface and does not get into contact like it is possible in the AM mode. For the frequency modulated method the cantilever is oscillating always at the resonance frequency f_{1st} but with a difference in the phase $\phi = 2\pi ft$ between resonance and excitation frequency of 90°. To realize this, a PLL (phase-locked-loop) is used. Locking on the phase, the time-resolved frequency, between excitation- and oscillation frequency the PLL controls the excitation amplitude A_{exc} in that way that the oscillation amplitude A is kept constant, when the force interaction between tip and sample is changing the oscillation frequency of the cantilever. The advantage of this mode is that in contrast to the AM-mode the time delay of the eigenfrequency and so also for the distance controler does not dependend on the Q-factor. It is simply defined by $\tau = \frac{1}{f_{1st}}$ and

so, due to the possibility to use cantilevers with high Q and higher signal-to-noise ratio, much smaller force gradients can be detected, which makes the FM-mode much more sensitive than the AM-mode. Figure 3.2 shows an example of a schematic setup for the FM-mode with which the first true atomic contrast was achieved [29].

3.1.3 Frequency Shift and Forces in NC-AFM

So what is then the relationship between the frequency shift of a cantilever oscillation and the forces between a cantilever tip and the sample like shown above in Fig. 3.3? For this we have to consider the laws of the elasticity theory for a damped harmonic oscillator. In FM mode, which is mainly used for the experiments shown in the later chapters, the damping of the oscillator, meaning its frictional force, is compensated by the excitation or driving force of the cantilever. Therefore, the equation of motion can simply be written as:

$$m_{eff}\ddot{z} = -kz + F(z), \tag{3.3}$$

where m_{eff} is the effective mass and k the spring contant of the the cantilever. The vertical tip position z is defined as $z = z_0 + Asin(\omega t)$. This way to describe z is used for big amplitudes. In that case, the tip-sample interaction only has an effect on the harmonic cantilever oscillation in its lowest turning point. Therefore, the force acting on the tip is also oscillated by $sin(\omega t)$. The outcome of substituting z in equation 3.3 and a multiplication with $sin(\omega t)$ is:

$$-m_{eff}A\omega^2 sin^2(\omega t) = -kAsin^2(\omega t) - kz_0 sin(\omega t) + sin(\omega t)\ F(z_0 + Asin(\omega t)). \tag{3.4}$$

The integration of equation 3.4 over one oscillation cycle $T = \frac{2\pi}{\omega}$ results then in:

$$\begin{aligned} -\int_0^{\frac{2\pi}{\omega}} m_{eff}A\omega^2\ sin^2(\omega t)dt = \int_0^{\frac{2\pi}{\omega}} \big[&-kA\ sin^2(\omega t) - kz_0\ sin(\omega t) \\ &+ sin(\omega t)\ F(z_0 + Asin(\omega t))\big]\, dt, \end{aligned} \tag{3.5}$$

which can be written as follows:

$$\pi A \left(\frac{k}{\omega} - \omega m_{eff} \right) = \int_0^{\frac{2\pi}{\omega}} sin(\omega t)\ F(z_0 + Asin(\omega t))dt. \tag{3.6}$$

Because the undisturbed resonance frequency is defined as $\omega_0 = \sqrt{\frac{k}{m_{eff}}}$ eq. 3.6 is changing to:

$$Ak \left(\frac{1}{\omega} - \frac{\omega}{\omega_0^2} \right) = \frac{1}{\pi} \int_0^{\frac{2\pi}{\omega}} sin(\omega t)\ F(z_0 + Asin(\omega t))dt. \tag{3.7}$$

Assuming that the frequency shift Δf is much smaller than the resonance frequency ω_0 so that $\frac{1}{\omega} \approx \frac{1}{\omega_0}$ with $\omega = \omega_0 - \Delta\omega$, and by using $\omega = 2\pi f$, equation 3.7 can be simplified to [30]:

$$Ak \frac{\Delta f_{1st}}{f_{1st}^2} = \frac{1}{\pi} \int_0^{\frac{2\pi}{\omega}} sin(\omega t)\ F(z_0 + Asin(\omega t))dt, \tag{3.8}$$

which leads to a more generalized form for n oscillation cycles:

$$Ak \frac{\Delta f_{1st}}{f_{1st}} = \frac{1}{2\pi n} \int_0^{2\pi n} cos(\theta)\ F[z(t)]d\theta, \tag{3.9}$$

with $\theta = 2\omega t$ as the phase. Using equation 3.8 in a equivalent form, the integral on the right was determined by Guggisberg *et al.* assuming a smaller tip radius compared to the tip-sample distance at closest approach of the cantilever oscillation [31]. Hence, the relations of the cantilever frequency shifts to the different forces, which were discussed already in chapter 2, was determined as follows [31]:

Frequency shift due to van der Waals force:

$$\frac{\Delta f_{vdW}}{f_{1st}} kA = -\frac{A_H R}{6\bar{s}\sqrt{2\bar{s}A}}. \tag{3.10}$$

A_H is the Hamaker constant (q.v. chapter 2), R the tip radius and A the oscillation amplitude.

Frequency shift due to chemical force:

$$\frac{\Delta f_{chem}}{f_{1st}} kA = -\frac{U_0}{\sqrt{\pi A\lambda}} \sqrt{2} \exp\left(-\frac{s - s_0}{\lambda} \right). \tag{3.11}$$

Frequency shift due to electrostatical force:

$$\frac{\Delta f_{el}}{f_{1st}} kA = -\frac{\pi \epsilon_0 R (U_{bias} - U_{CPD})^2}{\sqrt{2\bar{s}A}}. \tag{3.12}$$

3.1.4 Energy Dissipation in NC-AFM

When a free oscillating cantilever with an amplitude A and a free excitation amplitude A_{exc0} is approached to a surface it is damped by the forces acting between the atoms of tip and sample. Therefore, a change in frequency shift but also in the amplitude is detectable. This results in a change of A_{exc0} into a dissipated excitation amplitude A_{exc}, because the amplitude PI-controller is programmed to keep the oscillation amplitude constant by increasing the excitation. How fast and sensitive the detection of the parameters like amplitude and frequency shift is, is beside the PI-gain parameters also depending on the quality factor Q of the cantilever (see Fig. 3.3). The higher the Q the lower the smallest detectable force gradient (equation 3.2) and the lower the dissipation like it can be described by the following equation for the total energy loss per oscillation cycle:

$$E_{ts} = E_0 \left[\frac{A_{exc}}{A_{exc,0}} - \frac{f}{f_{1st}} \right] \approx \frac{\pi k A^2}{Q} \left[\frac{A_{exc}}{A_{exc,0}} - 1 \right]. \tag{3.13}$$

Here, the assumption $\Delta f << f_{1st}$ is made which results in $\frac{f}{f_{1st}} \approx 1$. E_0 represents the intrinsic loss of energy per oscillation cycle, k the cantilever spring constant and Q is the quality factor of the free oscillating cantilever. Additionally recorded, the excitation A_{exc} gives extra informations about dissipative processes occuring between tip and sample like deformations of the surface or the probe [32] due to the van der Waals interactions [33].
Tip-sample interaction forces are not the only possibility of causing a damping of the cantilever oscillation. A phase shift which is set by the phase controller of the phase-locked-loop and which is differing from $-90°$ between the oscillation and excitation results in a higher excitation (see Fig. 3.2). Further source of dissipation is an uncompensated electrostatic force which induces image charges in tip or sample as well as a displacement currents resulting in a joule-dissipation whose strength is depending on the local conductivitiy [34].

3.2 Dynamic Force Spectroscopy

The problem in dynamic force microscopy can be explained by a closer look to equation 3.9 in the last section. For a conversion of the detected frequency shift Δf in DFM into force the integral to be used is only valid within the bounderies of 0 and 2π. Therefore, the strength of influence of longrange forces on the tip-sample system is needed in order to calculate the total force bewteen probe and sample out of the measured frequency shift. The only possibility to achieve such a conversion with a DFM is using dynamic force spectroscopy (DFS) and detecting the frequency shift or rather the force versus tip-sample distance. An inversion of equation 3.9 has to be done to get the final force values. While some mathematical approaches for the integral inversion are only performed for cases of very small or very large oscillation amplitudes [28, 35], a good ansatz is given by J. Sader and S. Jarvis *et al.* which is valid for arbritary amplitudes [36]:

$$F(z) = 2k \int_z^\infty \left[\left(1 + \frac{A^{1/2}}{8\sqrt{\pi(u-z)}} \right) \Delta\Omega(u) - \frac{A^{3/2}}{\sqrt{2(u-z)}} \frac{d\Omega(u)}{du} \right] du, \tag{3.14}$$

where $\Delta\Omega(z) = \Delta\omega(z)/\omega$. $u - z$ is the covered tip distance. Also, the potential between tip and sample can be calculated out of equation 3.14 resulting in:

$$U(z) = 2k \int_z^\infty \left[(u-z) + \frac{A^{1/2}}{4} \sqrt{\frac{u-z}{\pi}} + \frac{A^{3/2}}{\sqrt{2(u-z)}} \right] \Omega(u) du. \tag{3.15}$$

Using this algorithm, not only single force-distance curves can be made. Taking curves along a single line or even over a whole sample area leads to 2D or rather 3D spectroscopy fields of the investigated surface in real space. They show the evolution of the interaction force in dependence of the tip-sample distance [37, 38, 39]. In order to reduce high thermal drift between single spectroscopy curves, 2D and 3D fields are mainly done at low temperatures using liquid nitrogen (77 K) or even liquid helium (4 K). Combining the force field spectroscopy with the so-called atom tracking (AT) [40, 41] the drift between single spectroscopy curves can be minimized by tracking the position of an atom or defect as an reference point for the

spectroscopy paths [42, 43]. This technique enables to perform spectroscopy field mapping with a high data density even at room temperature and is used in the chapters 6 and 7 for the investigation of the surface stability and interaction forces as well as work function differences of h-BN and graphene.

3.3 Bimodal Dynamic Force Microscopy

In the last sections it was shown, that atomic scale contrast arises from short-range forces which are caused by covalent or ionic bonding [44, 45]. When using a monomodal DFM setup with amplitudes in the range of 10 nm, the frequency shift due to the usually stronger long-range forces is caused by the macroscopic tip shape as well as the electrostatic potential. By optimizing the tip geometry towards sharper tips, the influence of this background force or rather its disturbance of the short-range force detection can be reduced. Another approach, which increases the signal-to-noise ratio and the sensitivity to short-range interaction forces is simply the usage of amplitudes $<<$ 1 nm which are in the range of the decay length of the short range interaction. Probes for stable and small amplitude operation also need to have a high stiffness [46] which was for example realized in tuning-fork sensors [25]. Anyhow, the disadvantage of this sensor is its relative low Q-factor of $Q \approx 2000$. A good alternative to such sensors is the utilization of a higher flexural cantilever mode in a beam deflection AFM, like the second one with a resonance frequency of $f_{2nd} \approx 1$ MHz and a spring constant of $k_{2nd} \approx 1500 \frac{N}{m}$ being higher than that of the first mode. An additional profit of this method is a higher Q value ($Q \approx 5000 - 15000$) [47, 48, 49, 50, 43].
By using the 2nd flexural mode, the sensitivity towards short-range interactions is enhanced due to the use of smaller amplitudes. Therefore, imaging at larger tip-sample distances compared to measurements using the 1st flexural mode is possible. For a higher resolution the tip-sample distance has to be decreased. For smallest tip-sample distance at the lowest turning point of the tip oscillation path the formation and breaking of atomic-scale junctions may prevent stable operation. While imaging under these conditions remains challenging, recently 1D spectroscopy curves without jumps have been measured down to very small tip-sample but using arelatively big amplitude of ≈ 0.4 nm [51, 52]. The instabilities can be prevented, if the cantilever is excited simultaneously at the first and second flexural mode

($f_{1st} + f_{2nd}$) by employing a second PLL (phase locked loop). By this, the first flexural mode is used to stabilize the scan with $A_{1st} \approx 10\,nm$, and the second for the detection of the short-range forces with $A_{1st} \approx 100\,nm$, dominating at a tip-sample separation approximately corresponding to the lowest turning point of the oscillation of the 1st mode. A connection scheme for the bimodal detection with two PLLs is given in Fig. 4.8 of section 4.3.

The interpretation of a force detection by the second resonance frequency (f_{2nd}) is given by equation 3.9 in this chapter which is also valid for the ith resonance mode at n_i oscillation cycles [50, 51]:

$$A_i k_i \frac{\Delta f_i}{f_i} = \frac{1}{2\pi n_i} \int_0^{2\pi n_i} cos(\theta_i)\ F[z(t)] d\theta_i. \tag{3.16}$$

k_i is the effective stiffness of the ith mode like theoretically shown by Melcher *et al.* [53]. For the bimodal case with the two incommensurate frequencies f_{1st} and f_{2nd}, the motion of the tip is described by $z(t) = z_0 + A_{1st}cos(\theta_1) + A_{2nd}cos(\theta_2)$ whereas $\frac{\Delta f_i}{f_i} << 1$. In the case that $A_{1st} >> A_{2nd}$, Δf_{1st} becomes almost the same as for the monomodal case. The expansion $A_{2nd}cos(\theta_2)$ still contributes to Δf_{2nd} but averages to zero for first orders. Together with the assumption that the oscillation cycles limit by $n_2 \to \infty$ so that an integration of θ_2 over sequenced f_{1st} oscillation cycles is equal to a dense sampling over one single cycle ($n = 1$), equation 3.16 can be simplified to:

$$k_2 \frac{\Delta f_{2nd}}{f_{2nd}} \approx -\frac{1}{4\pi} \int_0^{2\pi} F'[z_0 + A_{1st}cos(\theta_1)] d\theta_1. \tag{3.17}$$

The short-range force contribution of $F' = dF/dz$ to Δf_{2nd} is much stronger than to Δf_{1st} because the force gradient F' has a faster variation compared to that of F itself. Excluding the first cantilever oscillation leads to the following correlation between force gradient and second resonance shift Δf_{2nd}:

$$k_2 \frac{\Delta f_{2nd}}{f_{2nd}} \approx -F'(z_0), \tag{3.18}$$

with $k_2 \approx 40 N/m$ [50]. A general time-averaged force gradient can be defined as:

$$-\bar{F}' \equiv k_i \frac{\Delta f_i}{f_i}. \tag{3.19}$$

This theoretical prediction has been proved by experimental data recorded in [50]. In the raw data from a bimodal measurement on a KBr crystal Δf_{1st} is converted to force using the Sader-Jarvis algorithm [36]. Derivation of the force ($F' = dF/dz$) leads to the force gradient. This is compared to the simultanous recorded Δf_{2nd} raw data resulting in Fig. 3.4.

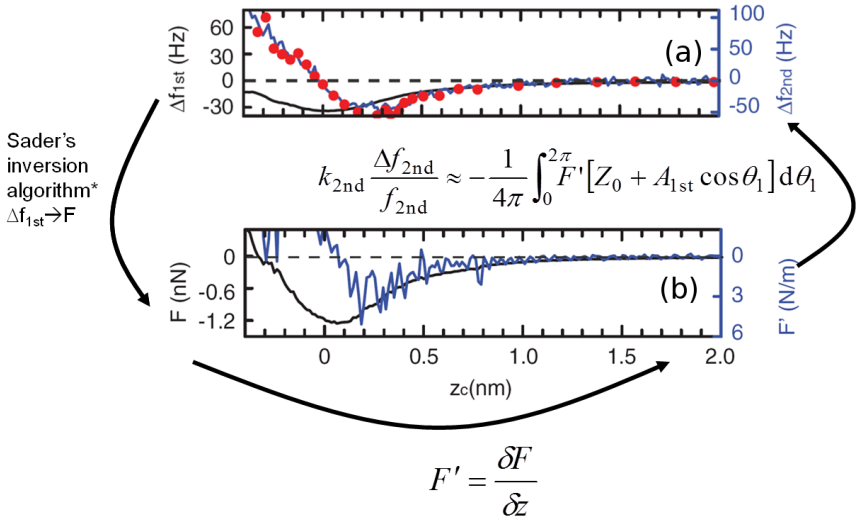

Figure 3.4: Prove of the time averaged force gradient [50]. $\Delta f_{1st}(z)$ and $\Delta f_{2nd}(z)$ measured on KBr. (a) shows the first (black) and second frequency shift (blue) versus distance. The red dots are calculated out of the force gradient in (b), which itself is calculated out of $\Delta f_{1st}(z)$ in (a) [36], proving the correctness of equation 3.19. $A_{1st} = 17.8$ nm and $A_{2nd} = 25$ pm.

As can be seen in the Fig. 3.4, the red dotted line fits almost perfectly to the $\Delta f_{2nd}(z)$ raw data from the measurement proving the accuracy of equation 3.19.

Not only the vertical modes can be used for microscopical measurements. The cantilever can also be excited laterally using the first torsional mode with a high sensitivity to lateral forces [54, 55, 56, 57, 43] like it is shown in Fig. 3.5. The torsional detection by normal cantilevers, using frequencies of about 1.5 MHz has to be run together with a vertical oscillation in bimodal mode, in order to control the tip sample distance. Nevertheless, for the interpretation of the torsional mode, the same ansatz as used for the second flexural mode above can be utilized. With $A_{1st} >> \lambda > A_{TR}$, where λ is the decay length of the lateral short-range interaction, it follows for the torsional mode analogue to equation 3.17:

$$k_{TR}\frac{\Delta f_{TR}}{f_{TR}} = -\frac{1}{4\pi}\int_0^{2\pi} F'_X[z_0 + A_{1st}cos(\theta_1)]d\theta_1, \tag{3.20}$$

where F'_X is the lateral interaction force gradient in th X direction.

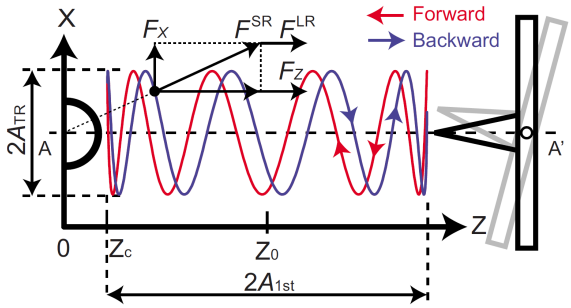

Figure 3.5: Scheme of the tip-sample interaction in bimodal DFM using torsional mode and the first flexural mode for tip-sample distance control [43]. The colored line are presenting the trajectories of the bimodal tip oscillation in forward and backward direction.

Using the algorithm by Dürig *et al.* [35], the lateral force gradient can be extracted from the torsional frequency shift Δf_{TR} as a function of the tip-sample distance:

$$F'_X = \frac{4k_{TR}}{A_{1st}f_{TR}}\int_z^{\infty}\sqrt{\frac{A_{1st}^3}{2(t-z)}}\frac{d\Delta f_{TR}(t)}{dt}dt. \tag{3.21}$$

With torsional modes, amplitudes of ≈ 40 pm and spring constants of about 2000 $\frac{\mathrm{N}}{\mathrm{m}}$ can be reached resulting in a high signal-to-noise ratio.

3.4 Kelvin Probe Force Microscopy (KPFM)

The work function of materials is a material specific energy needed to bring an electron from the solid state body across the surface (the Fermi edge E_F) to the vacuum level E_{vac}. The reasons for such an energy are of multiple nature. The surfaces of crystals have additional electron states which can be occupied by electrons (surface states). The surface charges are normally neutralized by the charges within a few atomic layers in the inner body, the so-called dipole layer. Its thickness depends on the amount of free charge carriers, so that the dipole layer is small for metals while its thickness is

increased for insulators, and influences the band bending of the conduction bands. Therefore, a disturbance of the electric field and by this also of the potential energy distribution by the surface charge separation due to the mentioned dipole layer is existing. On the other hand interactions (exchange and correlation interactions) of the valence electrons among each other as well as with the inner electrons of the atoms are also contributing to the work function [58].
In this chapter, a method for measuring the work function based on the Kelvin principle compbined with an AFM shall be presented and discussed. Other methods used to determine the work function like Photon Electron Spectroscopy (PES) will not be discussed, as they are not used for measurments done for this work.

3.4.1 The Kelvin Principle

The Kelvin principle is based on the work of (and also named after) Sir William Thomson, who was also known as Lord Kelvin. He used a plain capacitor made out of two metallic plates [59]. The variation of the distance of the plates by an oscillation ω within the electric field between the capacitor plates is resulting in a change of the capacitance ΔC, which induces a time dependent current $I_{CPD}(t)$. This current is defined as follows [60]:

$$I_{CPD}(t) = U\omega\Delta C cos(\omega t). \tag{3.22}$$

The voltage $U = U_{DC} - U_{CPD}$ can now be nullified by the variation of U_{DC} until the electric field between the plates is compensated which leads to $I_{CPD}(t) = 0$. The now determined CPD (U_{CPD}) leads, as long as the work function of one capacitor is already known, to the work function of the unknown plate by the use of [61]:

$$U_{CPD} = \frac{\Phi_1}{q} - \frac{\Phi_2}{q} \equiv \frac{\Delta\phi}{q}, \tag{3.23}$$

where Φ_1 and Φ_2 are the work functions of the capacitor plates and q is the charge of the charge carriers (for electrons: $q = -e$).

The AFM is build to detect forces. When combining the AFM with the Kelvin method for work function detections, so-called *Kelvin Probe Force Microscopy* (KPFM), the electrostatic force between tip and sample is de-

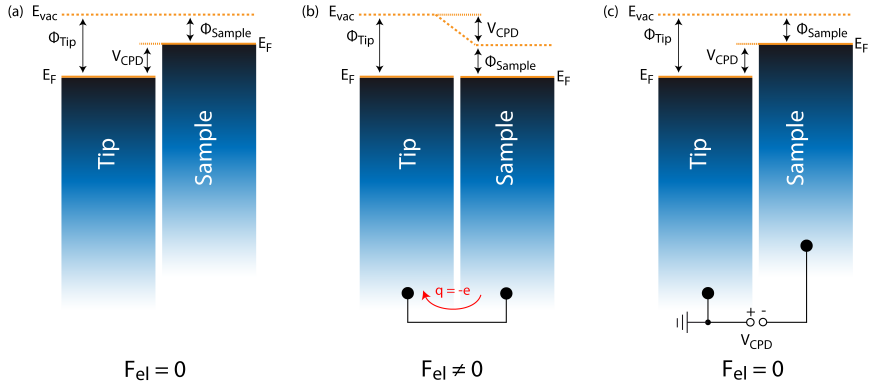

Figure 3.6: Definition of the CPD as well as of its measurement scheme.

tected, which can be approximated as a very small capacitor. This approach is more suitable than the detection of currents. Figure 3.6 shows a scheme of the detection method. If tip and sample are not connected (Fig. 3.6(a)), the vacuum energy levels (E_{vac}) of tip and sample are equalized, but their Fermi energies (E_F) are different by the value of U_{CPD}. Here, E_F of the sample is higher which results in a smaller work function Φ_{Sample} of the sample. If now tip and sample are electrically connected, a charge transfer from the sample to the tip leads to equilibrated Fermi-energy levels, whereas the vacuum energy level of the sample is lowered by U_{CPD}. This results in an electrostatic Force F_{ES}. This force depends on the capacity gradient of the capacitor plates (tip and sample) and can be described by equation 2.20 shown in chapter 2.3. Similar to the experiment done by Lord Kelvin, the distance between tip and sample varies due to an oscillation of the tip above the surface with the frequency ω by applying an AC voltage U_{AC}. Due to this, F_{ES} can be expressed by 3 separate components:

$$F_{ES} = F_{Cap} = -\frac{1}{2}\frac{\partial C(z)}{\partial z}\Delta\Phi_{el}^2 = F_{DC} + F_{\omega} + F_{2\omega}, \tag{3.24}$$

where $\Delta\Phi_{el} = U_0 + U_{AC}sin(\omega t)$ is the potential difference (voltage) between the capacitor plates and $U_0 = U_{DC} - U_{CPD}$. F_{DC} is the part of the force, which is related to an variable DC voltage U_{DC}, whereas F_{ω} and $F_{2\omega}$ are related to the AC voltage U_{AC}. Taking this all into account, together with 3.23 the three different force components can then be written as:

$$F_{DC} = -\frac{\partial C}{\partial z}\left(\frac{1}{2}\left(U_{DC} - \frac{\Delta\Phi}{q}\right)^2 + \frac{1}{4}U_{AC}^2\right), \tag{3.25}$$

$$F_{\omega} = -\frac{\partial C}{\partial z}\left(U_{DC} - \frac{\Delta\Phi}{q}\right)U_{AC}sin(\omega t), \tag{3.26}$$

$$F_{2\omega} = \frac{\partial C}{\partial z}\frac{1}{4}U_{AC}^2 cos(2\omega t). \tag{3.27}$$

If now the DC voltage U_{DC} is applied between tip and sample so that $U_{DC} = U_{CPD}$ as shown in 3.6(c), F_{ω} becomes zero, so that the total electrostatic force between tip and sample is reduced only to F_{DC} and $F_{2\omega}$. So, the oscillation of the cantilever with ω is stopped and only a statically bended cantilever due to F_{DC} is left. In addition, the $F_{2\omega}$ part can be used for capacitive spectroscopy as well as microscopy, like it is done by Abraham *et al.* in 1991 [62]. Equation 3.27 is mainly valid for a complete metallic capacitive system. This is limiting the measurable systems, so that for example for semiconducting samples a different definition of F_{ω} is needed, which was developed by Hudlet *et al.* [63]. They presented a way to express F_{ω} in dependence of the surface charge Q_s of the semiconducting sample, the dielectric constant ϵ_0 and the effective capacitance C_{eff} of the tip sample system in ambient conditions [61]. The result was:

$$F_{\omega} = \frac{Q_s}{\epsilon_0}C_{eff}U_{AC}sin\omega t. \tag{3.28}$$

For the determination of the sample work function Φ_{sample} it is important which part of the tip-sample capacitor is grounded and which is biased. A different sign has to be considered, depending if electrons or holes are needed to equalize the vacuum energy levels. By connecting tip and sample (Fig. 3.7(a)), the electrons are moving until equilibrium is reached. The fermi energy E_F is lowered. If the sample is biased like in Fig. 3.7(b) and the tip is grounded, a negative potential is applied, so that electrons are lifting E_F again. This case can be described as follows:

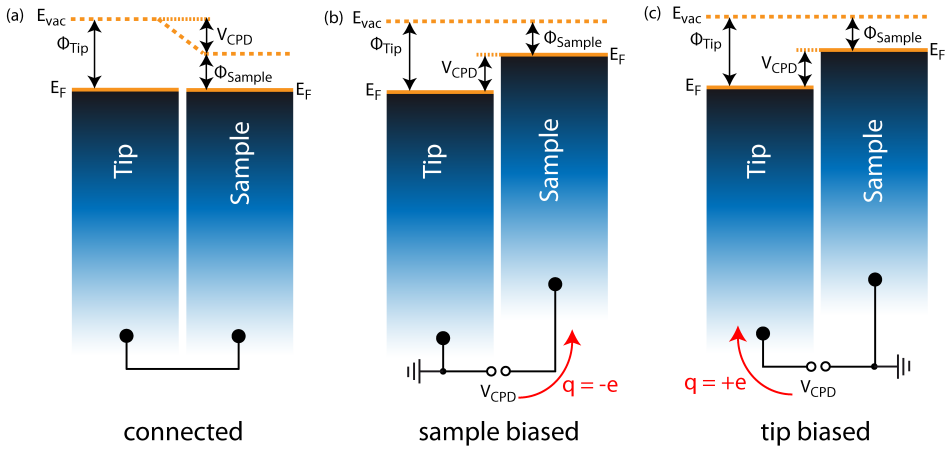

Figure 3.7: Illustration of the KPFM principle. Shift of the Fermi and vacuum energy levels due to a (a) connection of tip and sample, (b) a biased sample, and (c) a biased tip.

$$\Phi_{tip} - \Phi_{sample} = \Delta\Phi \tag{3.29}$$

$$\Leftrightarrow \Phi_{tip} - \Delta\Phi = \Phi_{sample} \text{ with } \Delta\Phi = qU_{CPD} \text{ and } q = -e \tag{3.30}$$

$$\Rightarrow \Phi_{tip} + eU_{CPD} = \Phi_{sample}. \tag{3.31}$$

If the sample is grounded (Fig. 3.7(c)) and the tip biased, holes are needed, which means $q = +e$. Equation 3.31 then changes to:

$$\Phi_{tip} - eU_{Bias} = \Phi_{sample}. \tag{3.32}$$

Equations 3.31 and 3.32 can only be used for the determination of the absolute work function out of U_{CPD} if the tip work function Φ_{tip} was calibrated before, equivalent to the method described above. Therefore, a metallic sample is needed, whose work function is already known.

The measurement of the U_{CPD} signal in KPFM can be done in two different ways with different sensitivity and signal-to-noise ratio. These two modes, frequency modulated (FM) and amplitude modulated (AM) KPFM, which will be presented in the next two sections, are mainly based on the same theory, shown above. Therefore, for a determination of work functions by

these two different detection modes, equations 3.31 and 3.32 are also valid.

3.4.2 Amplitude Modulated KPFM

The advantage of KPFM is the simultaneous detection of the sample topography and its work function with nanometer resolution or even less by the detection of the local contact potential difference (LCPD) which takes polarization effects into account [64, 65].
One detection mode in KPFM is the Amplitude Modulated Kelvin Probe Force Microscopy mode (AM-KPFM). In addition to the first resonance frequency f_{1st} the second resonance f_{2nd} is excited electrically by applying an alternating voltage U_{AC} with $\approx$1 MHz and an absolute value of $0.1 - 0.5$ V in order to detect the electrostatic force F_{el}. By this, its force component F_{ω} can be minimized to zero by adjusting U_{DC} [66]. A separation of the signals for topography and work function detection in AM-KPFM by using different resonance frequencies leads to a smaller bandwidth for the detecting lock-in amplifiers. This is increasing the signal-to-noise ratio, although the sensitivity of the second resonance due to a smaller Q-factor is lower than the Q of the first resonance. Nevertheless, using even higher frequencies for KPFM than f_{2nd} for an increased detection sensitivity is limited by the bandwith of the detector photo diode. However, effects of capacitive cross coupling can have an influence on the detection and can couple into the topography due to an uncompensated potential between tip and sample. Therefore, capacitive coupling has to be determined and minimized as shown in chapter 4.2.

3.4.3 Frequency Modulated KPFM

The second method used for measuring the contact potential difference, is the Frequency Modulated Kelvin Probe Force Microscopy (FM-KPFM). In this mode, the first resonance f_{1st} is additionally modulated by U_{AC} with a frequency of $\approx$1 kHz and an absolute value of $1 - 2$ V. Like in the AM-KPFM mode, the demodulation of the signal is done by a Lock-In amplifier [67]. Also here, atomic contrast is achieved [68]. Contrary to the AM method, in FM-KPFM the force is not detected directly. Instead, the force gradient is measured which has a high spatial resolution. It can be expressed

by

$$\frac{\partial F_\omega}{\partial z} = -\frac{\partial^2 C}{\partial z^2}\left(U_{DC} - U_{CPD}\right) U_{AC} sin(\omega t). \tag{3.33}$$

Because the first resonance for the detection is used, a higher bandwidth has to be chosen which is almost in the range of the AC modulation frequency. But a higher bandwidth is also related to a lower signal-to-noise ratio. Also, in comparison to AM-KPFM, higher absolute modulation amplitudes have to be chosen, which can also influence the topography signal of semiconductors by band bending [69].

Chapter 4

Experimental Setup

The premise for high quality microscopical measurements with atomical resolution is in a sense to have almost "*nothing*" on the surface, which means an ultra highly vacuumized environment. A pressure $< 10^{-10}$ mbar is the perfect condition not to contaminate the samples or the probes which leads to a longer measurement times and reduces scanning instabilities. Such a pressure is equivalent to a mean free path l of > 100000 km. This means an atom in the ultra high vacuum (UHV) has to fly in average approximately 100000 km until it hits another atom. Therefore, the probability to hit the walls of the vacuum chamber is much higher than that to hit another atom. The mean free path is defined by:

$$l = \frac{1}{\sqrt{2}\sigma n} \tag{4.1}$$

whereas $n = \frac{dN}{dV} = \frac{p}{k_B T}$ is the particle density in the volume V at pressure p and temperature T as defined by the ideal gas law in equation 2.1, and $\sigma = \pi(2r)^2$ is the scattering cross-section of the interacting atoms with r as the atomic radius [70]. By this the free path length can be expressed as

$$l = \frac{k_B T}{\sqrt{2}\pi(2r)^2 p} \ . \tag{4.2}$$

In order to reach and keep such low pressures inside a vacuum chamber, a combination of different pumps is used. A rotary vane pump provides a back pressure of approximately 10^{-2} mbar which is more than enough to run turbo molecular pumps. These kinetic pumps can pump the chamber down to a final pressure of $\approx 1 \times 10^{-10}$ mbar which is depending on their

pumping speed (*ltr./sec.*), the type of gas as well as the pump cross-section. Are lower pressures needed or has lighter gas to be pumped (hydrogen, helium, etc.) so-called adsorption pumps working by titanium sublimation or ion gettering are used to help to decrease the pressure to values lower than $\approx 1 \times 10^{-10}$ mbar. The other advantage of these pumps is, that they do not cause vibrations because they do not contain movable parts. By this, the mechanical noise level is decreased drastically.

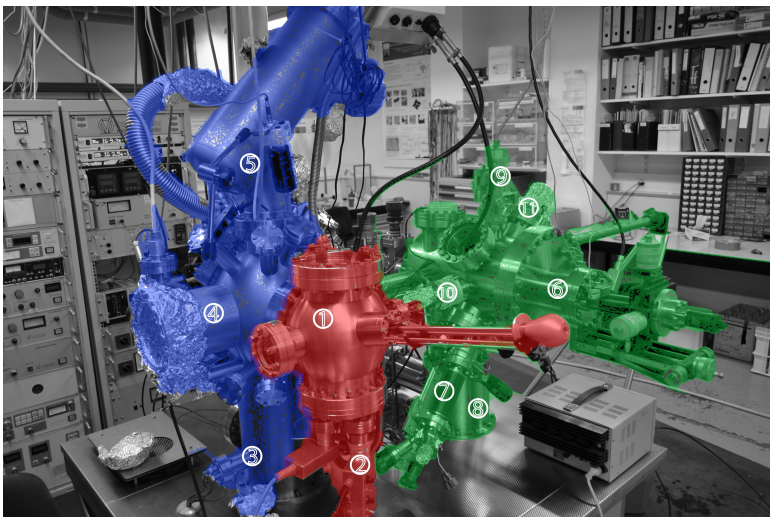

Figure 4.1: Overview of the UHV chamber. Microscope chamber (red): (1) AFM, (2) feedthrough and signal box. Analyzing chamber (blue): (3) Ti-sublimation pump and below the ion-getter pump, (4) LEED, (5) XPS. Preparation chamber (green): (6) manipulator with e-beam heating stage, (7) Knudsen-cell, (8) Ti-sublimation pump and below the ion-getter pump, (9) ion sputter gun, (10) quartz crystal micro balance (QMB), (11) quadrupol mass spectrometer (QMS).

Figure 4.1 gives an overview over the UHV system which can be divided mainly into three parts: the preparation chamber (green), the analyzing chamber (blue) and the part with the microscope itself (red). It is not separated from the analyzing chamber by a valve like between analyzing and preparation chamber. The single parts are listed in the caption of the figure 4.1. A part, which is not visible here, is the load lock situated beside the preparation chamber. It is used to introduce samples as well as probes. The transfer between load lock and preparation chamber as well as preparation- and analyzing chamber is done by mag-probe manipulators. In both chamber parts heating stages are attached. The preparation chamber

has an e-beam / resistive heater which reaches temperatures up to 1100 °C. The heater in the analyzing chamber is a normal resistive heater which reaches temperatures up to 300 °C. At the preparation chamber different sample preparations can be done. Apart from heating and sputtering using different gases (argon, nitrogen, etc.) there is the possibilty of evaporating molecules to the sample with a knudsen cell with a calibrated molecular flow by a quartz crystal micro balance. In the analyzing chamber, furthermore a LEED and XPS system are attached.

4.1 The Microscope

The heart of the UHV chamber is the microscope. It persists of a framework in which a platform is suspended by four springs. Additionally, an eddy current or rather hysteresis damping system is attached for a better decoupling from mechanical noise.

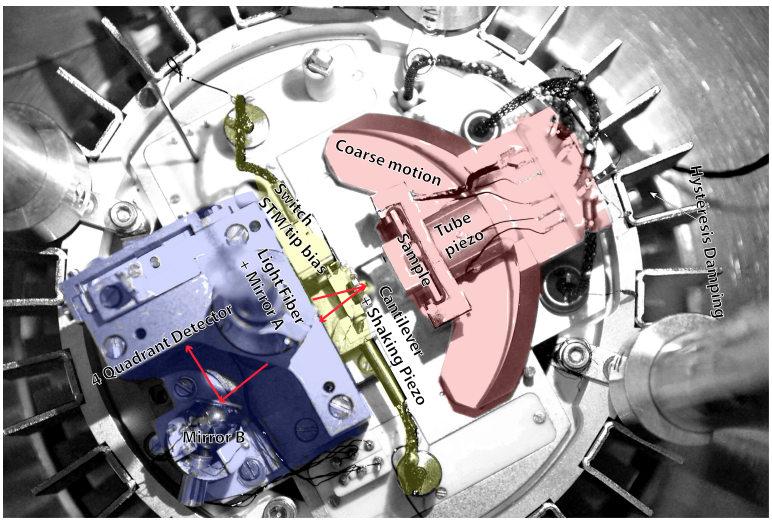

Figure 4.2: The room temperature AFM used for the measurements in this work. It is a further development of [71]. Red: the coarse motor with the (x, y, z)-piezo scanner and the sample holder. Blue: Part with the photodetector, the mirrors and the light fiber. Yellow: Cantilever holder, preamplifier with switch for STM and tip-bias mode. The red line marks the path of the laser beam. The fins surrounding the platform are part of an eddy current or rather hysteresis damping.

The AFM is imaged in detail in Fig. 4.2 and 3 sections are highlighted by different colours. The blue section contains the parts needed for the optical

readout. Hereby, a gold coated glass fiber, introduced from outside into the UHV chamber, is transmitting the LED light through an integrated optic to mirror A, placed exactly below the fiber output and not being visible in Fig. 4.2. Mirror A, which can be moved by a computer controlled piezo drive is reflecting the light beam onto the end of the cantilever following the red line in Fig. 4.2. It is then reflected back over mirror B to the four-quadrant photodetector with a bandwidth of 3 MHz, which is directly attached to the preamplifier. This is mounted in the yellow section including a switch for changing to STM (with a switchable resistor for 10 MΩ and 100 MΩ) and tip-bias mode. Additionally, in this section the shaking piezo is mounted, on which the cantilever holder is attached. The red part includes all parts related to the sample. The sample holder, surrounded by a copper shielding, is mounted on the Z-piezo tube, which is essential for the scanning process. It is directly steered by the Z-controler of the used Specs Nanonis control system [1] for controlling the tip-sample distance and is also moving the sample in X- and Y-direction during the scanning process. An extra wiring connects the tip to the bias line. The biggest part in the red section is the slider, which simply bears on 3 piezo motors for a coarse movement in horizontal directions as well as small in-plane rotations.

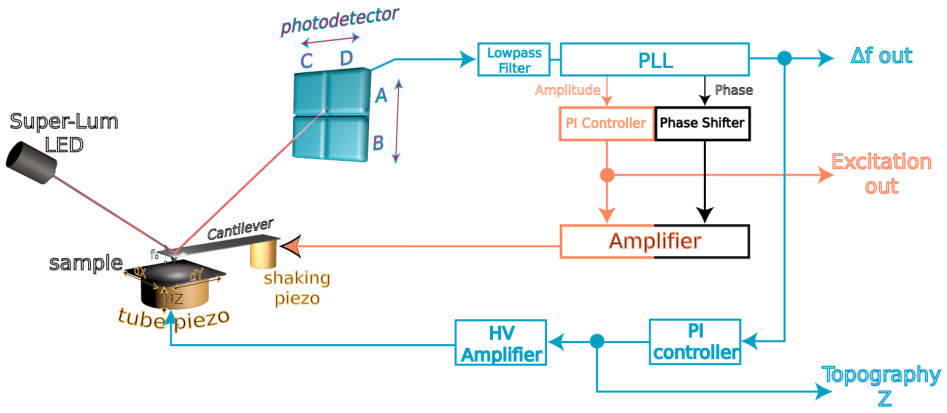

Figure 4.3: Instrumentation scheme for a dynamic force microscope operated in the FM mode using beam deflection.

The cantilever oscillation, situated in the blue part, is detected by a beam detection system [23]. The oscillation signals collected by the photodiode (A-

[1] NANONIS, SPECS Zurich GmbH, www.specs-zurich.com

B; C-D) and transmitted over the preamplifier to the outside are processed by a Specs-Nanonis AFM readout and processing circuit. Latest is described in Fig. 4.3. In the normal nc-AFM mode, a Specs-Nanonis OC4 PLL (Phase Locked Loop) is used to lock on the first resonance frequency f_{1st} which together with its amplitude A_{1st} is kept constant by a feedback loop that is controlling the excitation of the cantilever with the shaking piezo. Is the tip approached to the sample, the resonance frequency is changing due to the interaction forces between tip and sample. This results in a shift of the phase as well as in a higher damping of the amplitude. This information from the PI-controller for the amplitude and phase shifter are used to determine the exact excitation to keep the oscillation constant. The PLL also determines the difference between actual resonance frequency and frequency shift setpoint. This Δf signal is used as the error signal for another PI-Controller which is steering the tube piezo in z direction. The so controlled tip-sample distance together with the actual x-y position on the sample is put out as the topography signal.

4.2 KPFM Setup

For determination of the work function the Kelvin principle is used as described in chapter 3.4.1. For a realization of this method, a system setup as shown in Fig. 4.4 is used, which is an extension of the nc-AFM setup shown in Fig. 4.3. The cantilever is excited at the second resonance by an AC voltage U_{AC} which is applied between tip and sample. The total oscillation of the cantilever is filtered by a highpass filter and the rest signal is then demodulated by a PLL that is used as an Lock-In (feedback off). The real part of the signal is then forwarded to the Kelvin controller, which is tuning a DC voltage $U_{DC} = U_{CPD}$ also applied between tip and sample so that the F_ω component in accordance to equation 3.27 is reduced to 0.

Before the described setup can be used, the Lock-In (PLL without feedback) has to be setted up which is explained by Fig. 4.5. The phase ϕ of the demodulated signal vector $\vec{R} = x + iy = R\exp(i\phi)$ is turned to 0 which minimizes the imaginary part of $\vec{R}$ also to 0. Thus, $\vec{R}$ becomes equal to $R = x$. The real value x, which contains the complete signal information, is then forwarded to the Kelvin controller, which minimizes x and subsequently also F_ω to 0 by applying a voltage U_{DC} to the bias line.

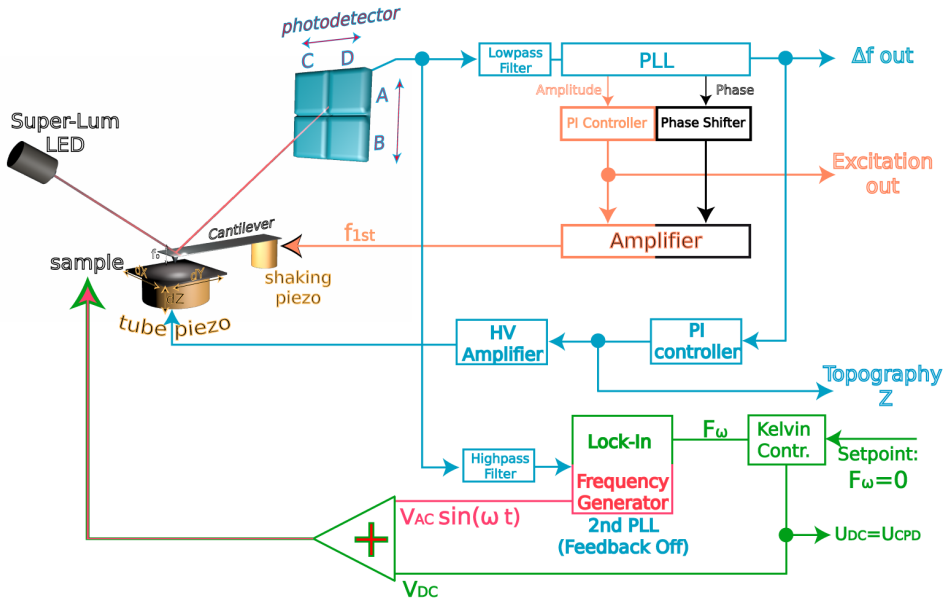

Figure 4.4: Instrumentation scheme for a dynamic force microscope used together with amplitude modulated KPFM.

Compensation of Capacitive Coupling

As mentioned by several groups, amplitude modulated Kelvin force microscopy, using the second resonance of the cantilever, can be influenced by capacitive crosstalk between the electrostatic excitation input and the deflection output signal of the four-quadrant photodetector (photodiode) [72, 69]. This cross talk is leading to an uncompensated electrostatic force between tip and sample, which can falsify the CPD or rather LCPD signal detected by the Kelvin setup. One possibility to reduce this capacitive coupling is to shield the signal lines inside the UHV chamber as well as using different feedthroughs for signal and bias lines [73, 69]. As shown by Diesinger *et al.* an additional active compensation of the cross talk by an external applied AC current reduces the crosstalk down to the noise level [74]. This AC current needs to have the same frequency as the electrostatic cantilever excitation and its phase and amplitude are fitted to the capacitive crosstalk measured between the four quadrant photodiode and the demodulator of the PLL. Figure 4.6 shows the power density spectra (PSD) of the 2nd frequency with half-logarithmic scale as it is detected by the photodiode with the light for beam deflection being switched off and the tip kept close

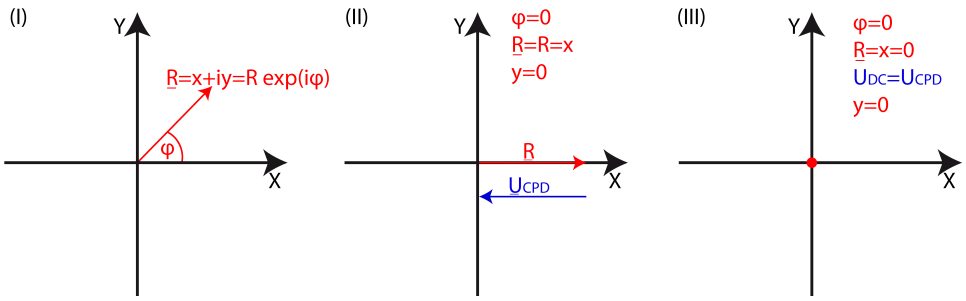

Figure 4.5: Illustration of how to operate AM-KPFM.

to the surface of a NaCl crystal. The black curve shows a clear crosstalk peak while it is vanished by switching on the compensation like for the red curve.

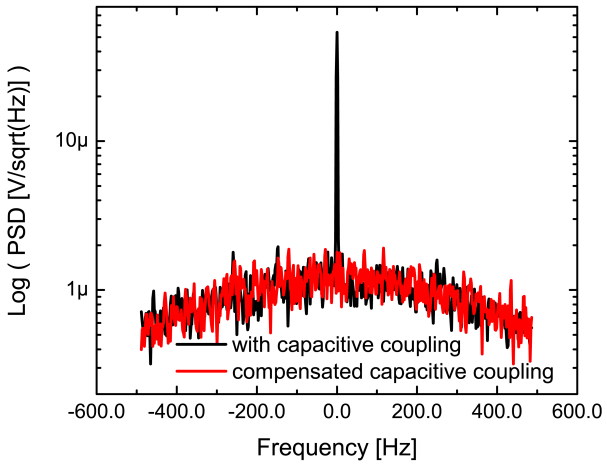

Figure 4.6: Example of a power density spectra of the capacitive coupling due to the electronic oscillation of the second resonance for AM-KPFM. Black: without cross talk compensation; red: with compensation.

In order to compensate the capacitive coupling the instrumentation scheme in Fig. 4.7 has to be used. A similar setup was already presented in [74]. For this, the tip has to be approached towards the sample and the tip-sample distance controller has to be switched off as well as the PLL feedback and the light from the Super-Lum LED for the beam deflection. With an external frequency generator, using the same time base like the PLL in order to avoid beat frequency, an AC voltage is applied. Phase and amplitude of this counter oscillation to the cross talk have to be adjusted so that

the peak in the PSD is reduced to the noise level as it is shown in Fig. 4.6. Here we additionally used an attenuator of 60 dB, to be able to apply very small oscillation amplitudes for the compensative signal which is then added to the deflection signal coming directly from the photodiode.

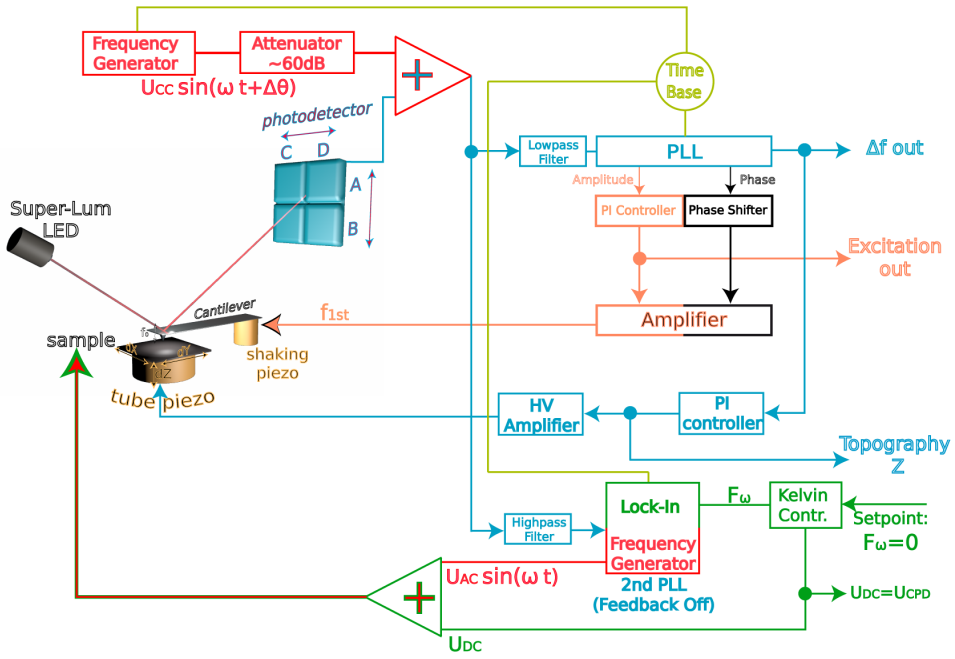

Figure 4.7: Instrumentation scheme for a dynamic force microscope with amplitude modulated KPFM and compensated capacitive coupling (CC).

It has also to be mentioned, that the effect of the capacitive coupling is smaller on metallic surfaces than on insulating ones due to the smaller DC and AC voltages needed for the compensation of the electrostatic forces as well as the CPD/LCPD of the sample. Therefore, the shown amplitude for the cross talk for a NaCl sample as shown in Fig. 4.6 is not representative in strength for a metallic surface.

4.3 Bimodal DFM Setup

In chapter 3.3 a way to icrease the sensitivity to vertical and lateral short-range interaction forces was presented as bimodal dynamic force microscopy. For the realization of this detection mode, the cantilever has to be excited at two incommensurate frequencies feedbacked over two simultanous operat-

ing Specs-Nanonis PLLs (OC4). One PLL, which is exciting the cantilever at the first flexural mode, is used for controling the tip-sample distance and recording the topographic informations like it is usual for the normal monomodal detection in nc-AFM. The second PLL, clocked internally at the same time-base signal, is exciting the second or torsional mode of the cantilever and is recording the frequency shift via a feedback-loop. Figure 4.8 shows an instrumentation scheme of the bimodal detection mode. Alternatively to the first flexural mode, the second resonance frequency can be used for controling the tip-sample distance which makes the use of higher amplitudes for the 2nd resonance necessary (≈ 0.1 nm).

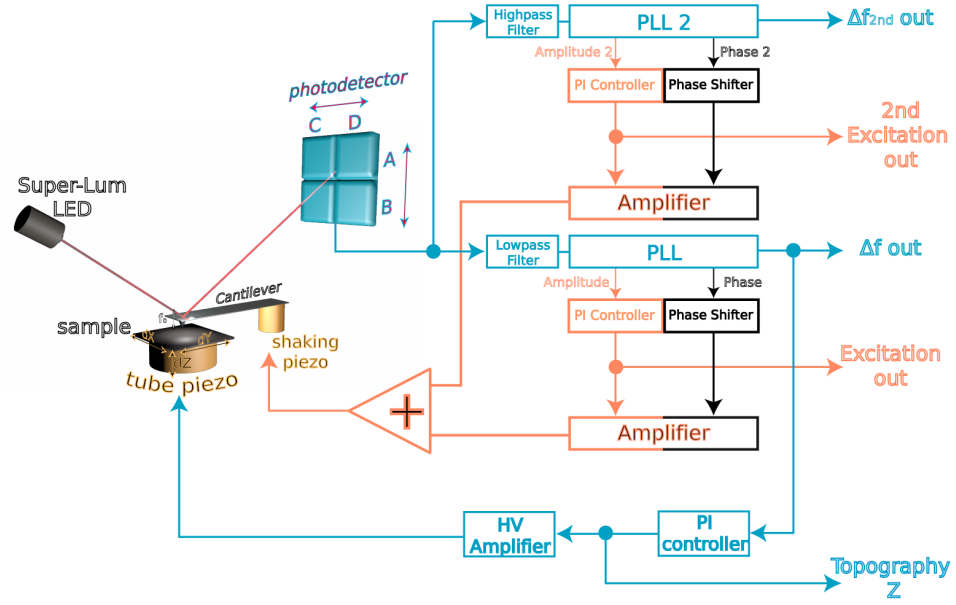

Figure 4.8: Instrumentation scheme for a beam deflection dynamic force microscope with bimodal excitation and readout.

4.4 2D Spectroscopy

As described in chapter 3.2 dynamic force field spectroscopy is a powerful tool to investigate the evolution of forces between tip and sample surface. For this thesis, the technique is used in order to record 2D force fields which will be presented in the upcoming chapters. Similar to the procedure used in [42], the atom tracking function [41, 40] of the Nanonis control

system was utlizied within our LABVIEW [2] spectroscopy program for accomplishing DFS measurements. This reduces the thermal drift and enables to acquire high quality force fields with an AFM operating at room temperature.

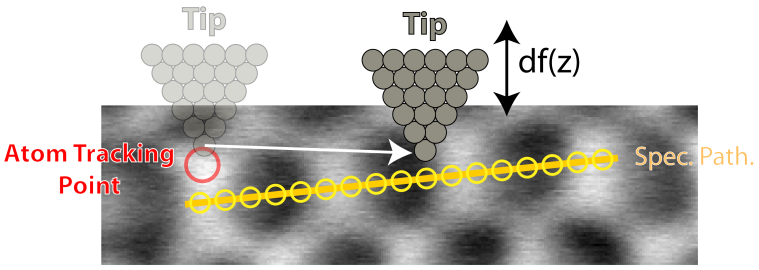

Figure 4.9: Illustration of the force field spectroscopy mapping procedure by the example of h-BN on Rh(111). While the atom tracking function tracks on a brighter defect (red circle) at the wire site, the spectroscopy path is followed, taking spectroscopy curves at 101 (for the h-BN) and 128 (for the graphene) positions. Every curve contains 512 points.

Figure 4.9 illustrates the procedure for mapping 2D spectroscopy fields by the example of the h-BN on Rh(111) superstructure. A set of adjacent single spectroscopy curves $\Delta f(z)$ is acquired proceeding along a predefined spectroscopy path. Between every two curves $\Delta f(z)$, the tip is tracked above a certain atom or defect chosen close to the path and being a reference for readjusting the (x, y, z)- position of the tip during the whole measurement. For the h-BN on Rh(111) this line contains 101 points while for the graphene on Ru(0001) 128 points are used. At each of this points single spectroscopy curves with 512 points resolution are taken. Before and after every 2D spectroscopy field, site-independent long range $\Delta f(z)$ curves are taken and connected to the site-dependent 2D data set at every spectroscopy curve. This procedure enables to calculate the force in dependence of the tip-sample distance by the Sader-Jarvis algorithm [36] as shown in chapter 3.2. For a later separation of the short range forces, by the procedure shown by Guggisberg *et al.* [31], the electrostatic force has to be eliminated by CPD compensation with a constant bias voltage applied between tip and sample.

[2] National Instruments, www.ni.com/labview

4.5 Multipassing Scan

A problem of comparing DFM images acquired at different setpoints (Δf) is the thermal drift as well as creep between subsequent measurements.By using the multipassing technique included in the Nanonis scan software, this problem can be minimized. Figure 4.10 illustrates this function. Contrary to a normal scan process, where after every completed measured image the setpoint is changed, the multipassing function allows to change the setpoint after every line. So, after one line is scanned in forward and backward direction, the first used setpoint is changed to the next defined setpoint scanning the same line again. This procedure is repeated until the last defined setpoint is reached. After that, the next line is scanned starting again with the first setpoint.

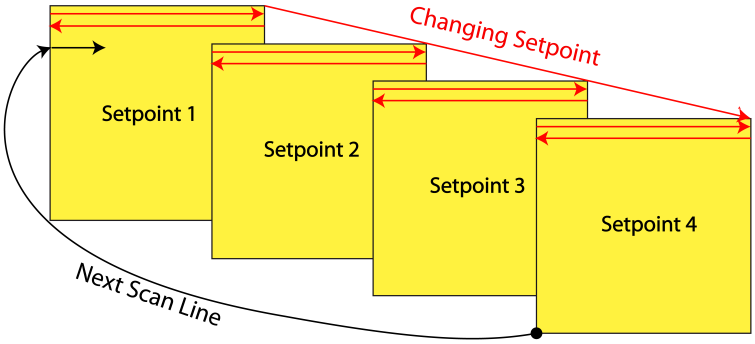

Figure 4.10: Illustration of the multipassing function implemented in the Specs-Nanonis scanning software.

By this way of data recording, the drift is minimized as well as the piezo creep which is reduced to the one occuring between the change from forward to backward scan direction.

Chapter 5

Preparation

5.1 Tip Preparation

In AFM, besides a sensitive and low-noise electronics a limiting factor for a high resulution detection is the probe, which is scanning above the surface. The probes, which are used for realizing non-contact AFM experiments, consist of a stiff cantilever bar ($k = 20 - 60\,\mathrm{N/m}$) with a conical tip at the end. The tips are edged out of a highly n-doped silcon chip with electrical properties preventing charging. Due to the metallic character, they allow also STM measurements as well as KPFM measurements. The tip radius has to be as small as possible, in order to ensure atomic resolution. The nominal tip size of the probes used in our experiments is below 10 nm. The cantilever's first resonance frequency f_{1st} varies around 170 kHz. Typical cantilever dimensions of the cantilevers in use, purchased from Nanosensors [1] are listed in table 5.1.

As shown in chapter 3 the advantage of the FM-AFM detection technique, used for the experiments in this work, is the utilization of high quality factors of the cantilevers. The way of fixing a cantilever chip on a cantilever holder influences the quality of the mechanical and if applicable electrical contact between both, and is crucial for achieving a high quality factor. Especially for bimodal dynamic force microscopy experiments, for which also the second flexural mode of the cantilever is used, the quality of the mechanical contact is strongly influencing the Q-value of the second resonance. Mainly, two different ways of fixing a cantilever on the holder

[1] NANOSENSORS, www.nanosensors.com

thickness t	7 ± 1 µm
width w	38 ± 8 µm
length l	225 ± 10 µm
tip height h	$10 - 15$ µm
res. freq. f_{1st}	$150 - 180$ kHz
Q-factor Q_{1st}	$20000 - 32000$
spring const. k_{1st}	$20 - 30 \frac{\mathrm{N}}{\mathrm{m}}$
res. freq. f_{2nd}	$0.98 - 1.05$ MHz
Q-factor. Q_{2nd}	$2000 - 15000$
spring const. k_{2nd}	≈ 1500 N/m

Table 5.1: Dimensions of the Nanosensors PPP - NCL Cantilevers.

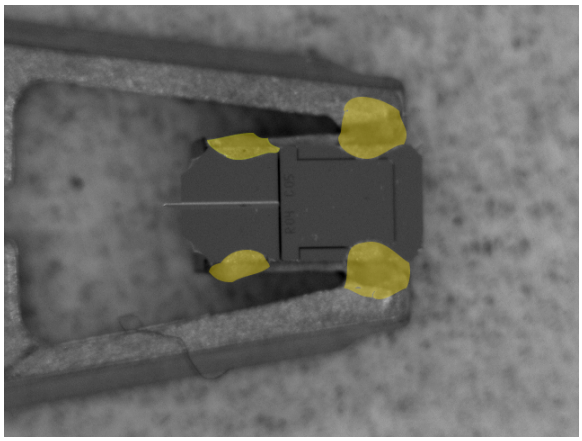

Figure 5.1: Foto of a cantilever glued with 4-point-glue-technique. The glueing points are colored yellow.

are used. One is using a metallic spring or cramp for fastening, which is probably the most fastest and reproducible way. The other method is based on glueing the cantilever chip on the holder. Although the reproducibility and the preparation speed of the cramping method is higher, the glueing method has its advantage in the flexibility of the cantilever types which can be used with the same cantilever holder. Also, the position of the probe chip on the holder can be varied and optimized easily in order to improve the Q-value which is the main reason why we are using the glueing method. Nevertheless, during the countless AFM measurements and experiments, many cantilevers had to be prepared. By this, the way of glueing cantilevers was improved, resulting in a four-point-glue technique shown in Fig. 5.1. The glueing points are made using the electrical conductive Epotek H20S

[2] glue, and are acting like springs pressing the cantilever down on the holder which is increasing the mechanical contact. The high amount of glue relative to the cantilever mass acts probably also like an additional weight which is reducing the loss of the cantilever excitation energy due to the oscillation of the chip. So, for the first resonance, a Q-value of up to 32000 and for the second resonance of up to 15000 are often achieved.
After glueing the cantilevers, the glue has to be dried which is done in an external oven at $\approx 120\,^{\circ}\mathrm{C}$ for $\approx 30\,\mathrm{min}$. After introducing the tip into the vacuum chamber, the probe as well as the holder has to be outgased, to avoid contaminations by water or leftovers of solvents in the glue. Contaminants on the tip of the cantilever after the first steps of preparation can easily be removed by $1-2\,\mathrm{min}$ of argon-ion sputtering with an accelaration energy of $680\,\mathrm{eV}$ and an argon gas pressure of $3\times10^{-6}\,\mathrm{mbar}$. Additionally coated tips should not be sputtered because the coating will be removed, so that the amount of glue should be reduced to a minimum.

5.2 Sample Preparation

For this work, single monolayers of hexagonal atomic structures on transition metals were created by chemical vapor deposition (CVD). The used metallic substrates of single crystals of rhodium (111) and ruthenium (0001) are known to be highly reactive and to have a strong catalytic activity. Therefore, before the substrate is exposed to borazine or ethylene which are the precursors for the formation of the hexagonal single layer systems, described here, the surface has to be cleaned thoroughly. This is done by several cycles of alternating Ar^{+}-sputtering, O_2-dozing at high temperatures, and subsequent annealing. The purity of the surface is then checked by AFM measurements. After the cleaning procedure, the hot metallic subrate is exposed to the precursor material (borazine or ethylene). Like that the hydrogen bonds of the precursors are cracked, a monolayer structure is formed and H_2 gas is desorbed. After the growth of one monolayer h-BN as well as graphene, the growth is saturated which can be explained by the reduced catalytic activity of the covered transition metals [75]. A non-optimal preparation can result in a non-regular grown diffraction pattern which is shown in Fig. 5.3

[2] Epoxy Technology, Inc., www.epotek.com

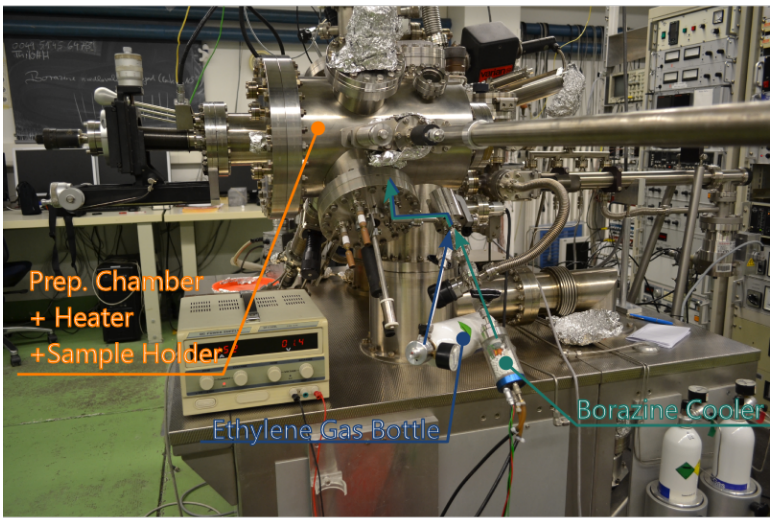

Figure 5.2: Image of the preparation chamber highliting the important parts for the preparation of h-BN and graphene.

using the example of graphene grown on ruthenium. The parameters for the preparation of h-BN and graphene layers are of course different from each other and are described more detailed within the next two subchapters.

5.2.1 *hexagonal* Boron Nitride on Rhodium (111)

For the preparation of the h-BN nanomesh on a Rh(111) crystal as well as on a Rh(111) thin film sample, borazine ($H_6N_3B_3$) is used which is an inorganic molecule consisting of three alternating untis of HB and HN arranged in a hexagonal ring (see Fig. 5.4 (a)). Keeping it in the liquid state at around $0 - 5\,^{\circ}\mathrm{C}$ in a crucible within a Peltier cooled device attached at the prepapration chamber (Fig. 5.2) helps increasing its lifetime [3]. Before the exposure of borazine on the Rh(111) surface, the borazine has to be cleaned from impurities and dirt. This is done by unmounting the peltier cooling device and freezing the borazine crucible by dipping it into liquid nitrogen. The liquid borazine then becomes solid. Increasing the temperature for example by the body heat starts outgasing the impurities out of the borazine. Then, the borazine has to be frozen again in order to pump the impure gas concentrated on top of the borazine. For this the valve to the pumping line

[3] private communication Th. Brugger, Univ. Zurich

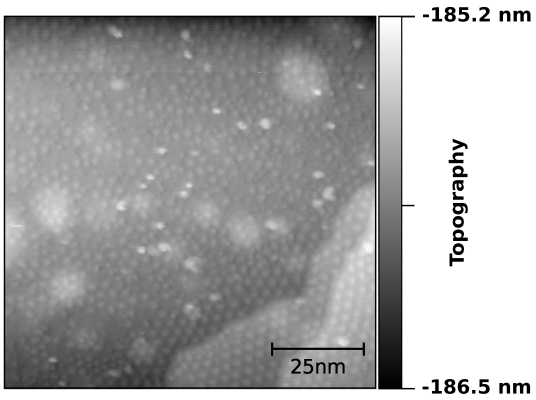

Figure 5.3: Non-regular grown graphene superstructure on Ru(0001) due to wrong preparation parameters or surface impurities.

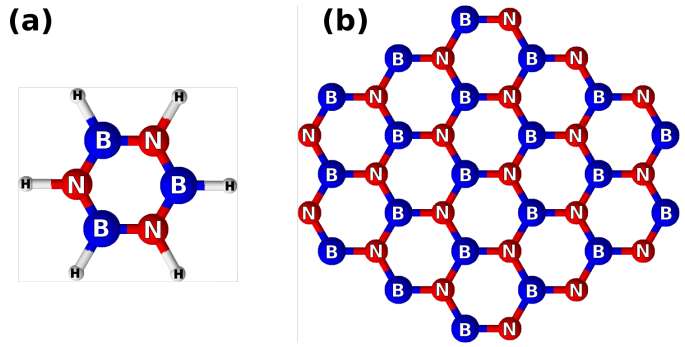

Figure 5.4: Schematic drawing of (a) borazin and (b) a sheet of *hexagonal*-boron nitride.

has to be opened slowly. This procedure should be repeated about 3 times in order to be sure to have highly pure borazine for evaporation.

Prior to the nanomesh formation, an atomically clean rhodium surface has to be prepared by alternating cyclces of 30 min *Ar*-ion sputtering on the substrate at room temperature and with an argon pressure of $p = 3 \times 10^{-6}$ mbar, 30 min of annealing at 750 °C, 10 min of O_2-dozing with a pressure of $p = 4 \times 10^{-8}$ mbar at a sample temperature of 450 °C, and another annealing cycle for 30 min at 750 °C. For the formation of the h-BN nanomesh, the rhodium substrate was kept at 790 °C during borazine exposure. For the preparation of our samples an exposure time of 3 min at a pressure of 3×10^{-7} mbar corresponding to 40.5 Langmuir was used.

5.2.2 Graphene on Ruthenium (0001)

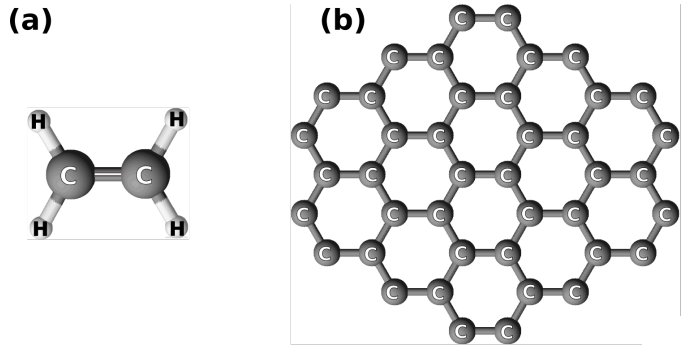

Figure 5.5: Schematic drawing of (a) ethylene and (b) a sheet of graphene.

Similar to the *h*-BN nanomesh on Rh(111), the preparation of a graphene monolayer on Ru(0001) [76] needs a thorough cleaning of the substrate, first. This was achieved by several cycles of 20 min Ar-ion sputtering at $p = 3 \times 10^{-6}$ mbar and annealing at T = 1100 °C for t = 40 min followed by an additional oxygen dozing ($p = 4 \times 10^{-8}$ mbar, T = 1000 °C, t = 40 min) and a final annealing at T = 1100 °C for again t = 40 min. After this procedure the ruthenium is ready for the exposure to ethylene gas (see Fig. 5.5 (a)) from the small 5 liter gas can attached to a needle valve at the preparation chamber as shown in Fig. 5.2. With a sample temperature of T = 1000 °C, an ethylene gas pressure of $p = 1 \times 10^{-7}$ mbar and a exposure time of 10 min corresponding to 40 L a graphene monolayer is formed (see Fig. 5.5 (b)). After stopping the exposure, the sample was again flashed by heating to 1100 °C for 1 min and then cooled down to room temperature by switching off the heater.

Chapter 6

Hexagonal Boron Nitride on Rh(111)

A great challenge in nanotechnology is the functionalization of surfaces and the creation of regular patterns with a long-range order for visionary electronic devices. A promising template for this purpose is the so-called hexagonal boron nitride (h-BN) nanomesh, a two-dimensional graphene like sp^2 hybridized monolayer, found to grow on Rh(111) [77], Ru(0001) [14] as well as on other substrates [78, 79, 80, 81]. With a periodicity of 3.2 nm it is grown as a large regular mesh of two different sites: holes and wires. The holes of the nanomesh have an inner diameter of ≈ 2 nm and are perfect for the purpose of forming large regular arrays with trapped molecules [14, 15, 82]. Even when using very low coverages the investigations of molecules on other substrates like NaCl or KBr can still be influenced by interactions with their next neighbours [83, 84] making the use of low temperature setups necessary [4]. Here, the h-BN nanomesh can open the door for investigations of decoupled, single molecules, which are separated from each other on the nanometer scale. Regular magnetic structures formed by nano particles like cobalt clusters are already realized on this material [12, 13] being a proper step towards the development of for instance new data storage devices with a large storage density.

In this chapter, high resolution DFM and DFS measurements of the h-BN are presented showing a highly regular superstructure as well as its atomic corrugation. In contrast to the conductive 2D graphene shown in the next chapter, h-BN is an insulating two-dimensional layer with a bandgap of

5 eV. The nanomesh super structure formed after performing the process presented in chapter 5.2 is due to a lattice mismatch of (13 × 13) B-N units to (12 × 12) rhodium atoms [77, 85, 86, 87]. Anyhow, sometimes the contrast observed during measurements appeared inverted. The occurance and origin of this contrast inversion as well as its influence on KPFM work function determinations will be discussed by analyzing the first 2D spectroscopy fields ever performed above this surface. Furthermore, Kelvin probe force microscopy images as well as 2D KPFM spectroscopy maps, combining the 2D DFS mapping with the KPFM method, are shown in order to determine the site dependent work function but also to discuss the influence of the topographical inversion on the work function.

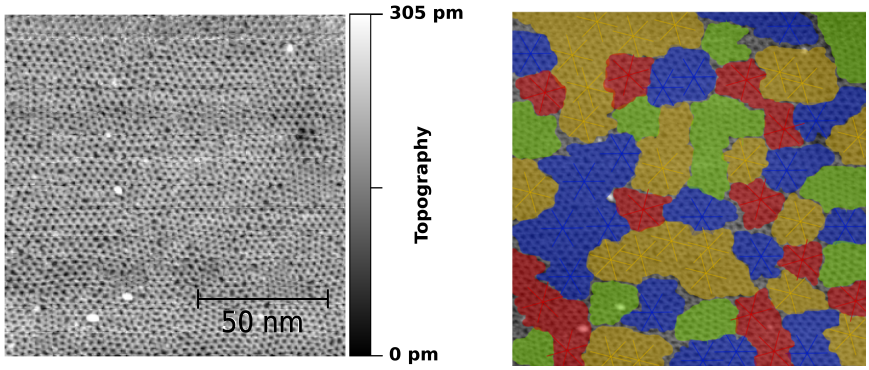

Figure 6.1: Left: Overview of the *h*-BN on Rh(111) sample. Right: Cropped area. 4 differently oriented domains were observed, which are coloured differently [88]. The *h*-BN growth is starting at several points forming hexagonal cells which then grow together to complete a monolayer. Scan parameters: f_{1st} =153 kHz, A_{1st} =5 nm, Δf_{1st} =−8.5 Hz, U_{Bias} =−32 mV.

Figure 6.1 shows a DFM topography image of the *h*-BN nanomesh on Rh(111). The hole- (dark) and the wire sites (bright) are clearly visible. A few adsorbates appear as bright spots on the completely covered area. Only within small domains of approximately $10 - 50$ nm, the observed superstructure grows with a regular orientation, whereas also the mesh size seems to vary. Dong *et al.* in [89] reported in more detail about the formation of the nanomesh and observed that the growth of *h*-BN on rhodium (111) during the CVD process starts simultaneously at many different positions on the metal surface and forming small patches or island-like domains of boron nitride which are growing together. The border lines of initially separated

domains are featuring a misalignment. In the right image in Fig. 6.1, different domains are marked by their different rotation. Mainly four different rotational domains were found which are completing the single monolayer. Due to the lack of atomic resolution measurements showing the rhodium substrate and the *h*-BN overlayer simultaneously, so far no conclusion about the exact orientations of the *h*-BN domains with respect to the underlying substrate for figure Fig. 6.1 can be drawn. However, Dong *et al.* [89] stated that the probability that any two islands with exactly the same orientation are matching is as low as 1/144 due to the underlying 12×12 Rh(111) unit cell. In consequence, the islands can be stretched and skewed on the one hand leading to different mesh sizes but probably also to our observed rotational domains in Fig. 6.1 on the other hand.

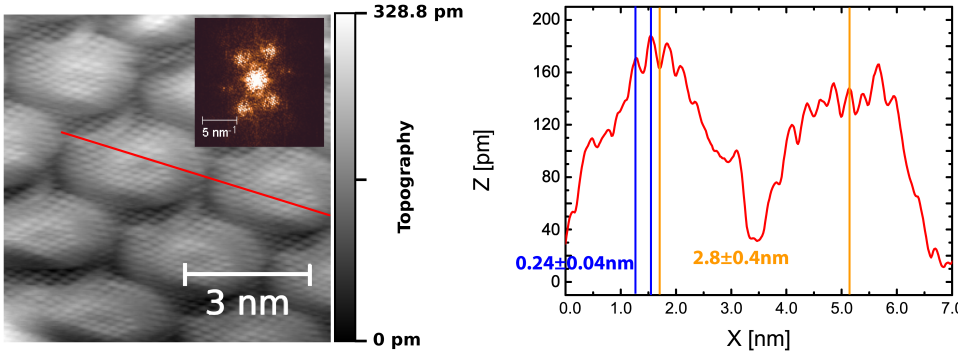

Figure 6.2: High resolution measurement of the *h*-BN. The corrugation of the nanomesh superstructure is inverted compared to the theoretical model [86, 87] but its atomic structure is clearly visible. Scan parameters: f_{1st} =156 kHz, A_{1st} =6 nm, Δf_{1st} =−180 Hz, f_{2nd} =973 kHz, U_{AC} =500 mV, U_{CPD} =−150 to − 30 mV.

Figure 6.2 presents a highly resolved measurement of the *h*-BN superstructure on Rh(111) showing for the first time atomic resolution achieved by nc-AFM. The CPD was compensated by simultaneously performing KPFM and was in a range of −30 to − 150 mV. The observed contrast is inverted compared to that presented in Fig. 6.1, which is expected from literature [86, 87]. A detailed investigation of this inversion will be presented in the next section of this chapter. The periodicity of the superstructure is determined after performing a Fourier filter transformation (FFT) with the analysis software WSxM [90] and is measured to be (2.8 ± 0.4) nm. The lattice constant of the atomic structure is 0.24 ± 0.04 nm. The relative big

errors for both periodicities are caused by piezo creep mainly dominant in the fast scan direction. Taking this into account, the determined values are still in good agreement with those determined in other experimental studies or theoretical calculations, which are $3 - 3.2\,\mathrm{nm}$ for the superstructure and $0.25 - 0.27\,\mathrm{pm}$ for the atomic periodicity [14, 12, 77, 82, 91, 75, 87, 92] where the last value corresponds to the hexagonal atomic lattice distance of the h-BN.

6.1 Contrast Inversion

Frequently, a contrast change in the recorded topography channel is observed, so that the prior superstructure of a depressed hole site and an elevated wire site is apparently inverted. The former holes then appear as elevations while the wires are lowered. This inversion of the contrast was also observed in scanning tunneling microscopy experiments where it was related to the bias voltage between tip and sample at a constant current, which corresponds to two different tunneling states for hole or wire [14, 12]. This results from a sigma band splitting due to different binding energies between boron, nitrogen and rhodium for every site. Due to the different quantities detected, the contrast inversion observed in AFM is not necessarily equal to the one observed in STM. While AFM is sensitive to the detection of short- and long-range forces acting between tip and sample, in STM the tunneling current, which strongly depends on the overlap of density of states of the tip-sample system, is measured. Fig. 6.3 shows the topography of the h-BN above an area of $50 \times 50\,\mathrm{nm}^2$. This image was scanned from bottom to top. For a continuous compensation of the electrostatic forces, KPFM is used showing a variation of the CPD of $\mathrm{U_{CPD}} = 108 - 1400\,\mathrm{mV}$. The lower part of the image shows the "normal" contrast until a spontaneous contrast inversion occurs. Thereafter, the contrast becomes sharper, showing the hole sites as elevations and the wires lowered. Closer to the upper end of the image, the contrast changes back to the "normal" one, probably induced by the adsorbate which is imaged as a bright spot at the top of Fig. 6.3. After passing the adsorbate the contrast switches again.

In order to investigate the event of the contrast inversion, the area indicated by the red rectangle in Fig. 6.3 was magnified (Fig. 6.4). There, the point of contrast inversion in forward (a) and backward (b) fast scan direction is

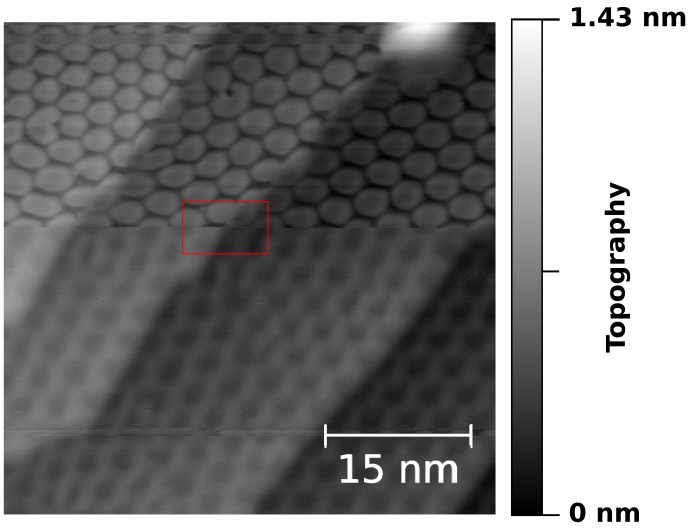

Figure 6.3: Topography image showing three contrast inversion events, the first one being marked by the red rectangle. Scan parameters: f_{1st} =155 kHz, A_{1st} =6 nm, Δf_{1st} =−75 Hz, f_{2nd} =962 kHz, U_{AC} =500 mV, U_{CPD} =108 − 1400 mV.

shown in more detail. The topography (left) and dissipated energy (right) images have a size of $9.8 \times 4.9\,\mathrm{nm}^2$. For the topography image in forward direction the position in which the contrast inversion occured is indicated by the circle. The line sections in Fig. 6.4(c) are taken exactly along the scan line of the contrast change. The position of the flipping is tagged by a vertical line. At that position, the topography signal was reduced by approximately 30 pm. In the dissipation channel, very close to the noise level of the measurement a slight increase of ≈ 20 meV/cycle is observed. In the top region of Fig. 6.3 the tip condition changes again while the tip is scanned above an undefined cluster on the surface. After some lines, the contrast inverted back again, showing the reversibility of the tip apex condition.
For the understanding of the inversion process as observed in Fig. 6.3 and 6.4 mainly two observations have to be taken into account. The adsorbate in the upper part of Fig. 6.3 is leading to an increased tip-sample distance due to the z-controller feedback of the AFM. On the other hand, such a distance dependent contrast inversion can be excluded by the interpretation of the dissipation- and the topography images in Fig. 6.4, which show only a slight tip modification at the point of inversion. Contrast inversions in the topography in nc-AFM were already observed and explained for different substrates

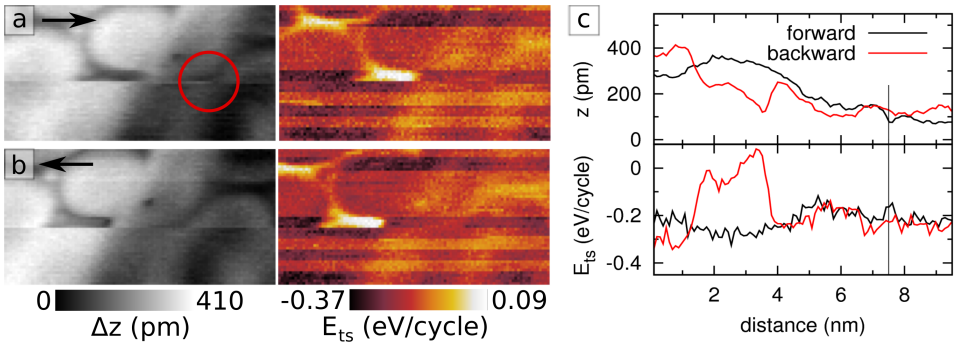

Figure 6.4: Enhanced images with a size of $9.8 \times 4.9\,\mathrm{nm}^2$ of the topography (left) and dissipation (right) in forward (a) and backward (b) direction taken from Fig. 6.3. Close to the center of the measurement shown in (a) the contrast change occurred as is indicated by the red circle. On the right line sections containing a profile of each channel, exactly matching the line of the tip change, are plotted.

indicating a major role of the long range electrostatic forces [93, 94, 95]. In the case of the rutile TiO2 surface for example, various different contrasts were found and the origin of an inversion process was theoretically described by a change of the tip polarity strongly influencing the detected force field in nc-AFM [96]. In the case of h-BN, such small tip apex modifications with a change of the tip polarity are one possible explanation approach for the inversion.

Nevertheless, if the contrast change is mainly influenced by a variation of the tip-sample distance it has to be controllable during the measurements. In Fig. 6.5 a multipass measurement for 4 different distances is presented. For the measurement with this method, which was described in detail in chapter 4.5, four different frequency shift setpoints ($\Delta\mathrm{f} = -4$ to $-8\,\mathrm{Hz}$) were chosen which are corresponding to four steps in the evolution of normal and inverted contrast. Due to the fact that the drift between the images is minimized to less than the range of the piezo creep differences in the fast scanning direction, the four images can be directly compared to each other. At $\Delta\mathrm{f} = -4\,\mathrm{Hz}$ the superstructure is imaged with its normal hole-wire contrast. With decreasing Δf setpoint and accordingly a decreasing tip-sample distance, the elevations start to appear indented or rather begin to invert. At $\Delta\mathrm{f} = -6.1\,\mathrm{Hz}$ the holes are still visible but the wire sites are starting to appear lower than the hollow sites. Finally at $\Delta\mathrm{f} = -8\,\mathrm{Hz}$ the wires are

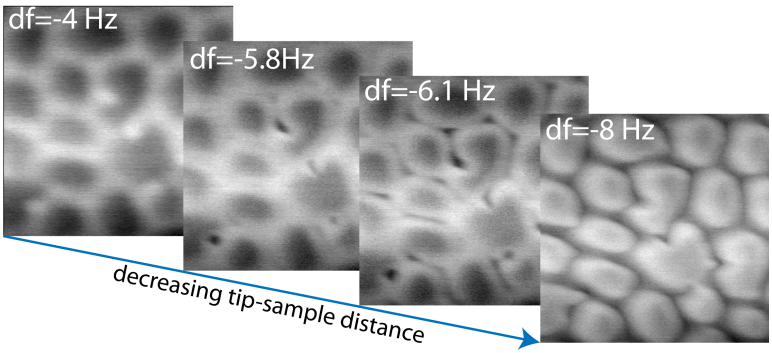

Figure 6.5: Four topographic images of h-BN on Rh(111) (14 nm×14 nm) recorded with the multipassing technique at different frequency shifts $\Delta f = -4$ Hz,-5.8 Hz,-6.1 Hz and -8 Hz respectively. For a continous compensation of the electrostatic force, KPFM was used. Parameters: A = 10 nm, $U_{CPD} = -386 \pm 45$ mV, $U_{AC} = 500$ mV.

imaged as depressions while the former holes changed to elevations.

Fig. 6.6 shows the evolution of the contrast inversion in a line section done across a hollow site. The lowest parts of the holes visible in the curves are aligned to z = 0 nm. Obviously, the shapes of the curves around the center of the holes are matching perfectly. Interestingly, the red curve ($\Delta f = -8$ Hz) shows that the wire site is the only area which is changing. While for the black curve the contrast is still "normal", for the green and blue curve a slight evolution towards the inverted is visible at the left peak located at approximately 1 nm. The change in distance for the wire site is roughly ≈ 110 pm. Overall, Fig. 6.5 and 6.6 are leading to the assumption that a distance dependent tip-sample interaction is the main factor of inversion. Furthermore, the possibility of a mechanical deformation induced by the tip should be considered as an explanation approach.

For a further study of the inversion mechanism, dynamic force spectroscopy measurements were carried out. Figure 6.7 shows 2D spectroscopy maps which are done by the procedure described in chapter 4.4. Inset curves for every 2D map, which are averaged over 3 curves per different site, are made to guide through the spectroscopy maps. The black curves correspond to the hollow- and the red curves to the wire sites. A constant bias of U_{Bias} =-500 mV is applied between tip and sample for compensating the electrostatic forces. Figure 6.7(a) presents a spectra of the total force

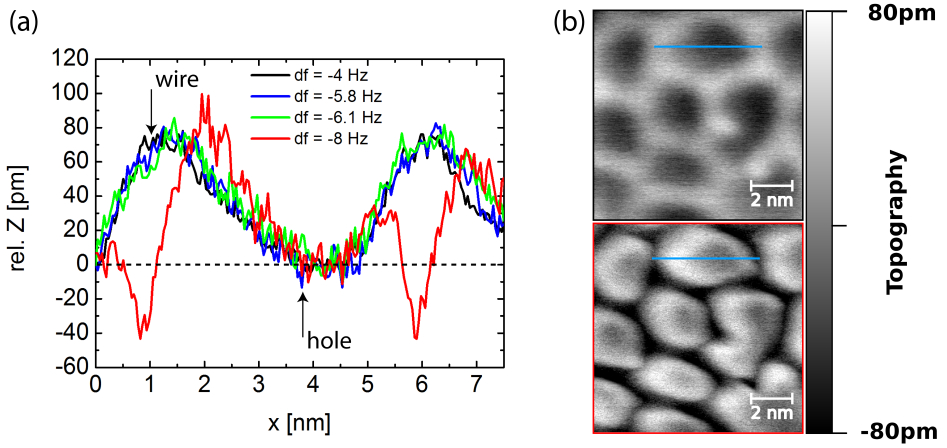

Figure 6.6: Detailed view of the contrast inversion of h-BN on Rh(111) recorded by the multipassing technique presented in Fig. 6.5. The cross sections in (a) taken along the fast scan direction show the development of the multipassing measurement for the hole and wire site marked in (b) by a blue line. The lowest parts of the holes visible in the curves are aligned to z = 0 nm. The height variation of the wire site with respect to the hole site is can be given in relative units: the total change between normal (Δf = -4 Hz) and the inverted contrast (Δf = -8 Hz) is $\approx$ 110 pm.

F between tip and sample. For the extraction of the force from the Δf raw data, the Sader-Jarvis algorithm [36] was used, which was introduced in chapter 3.2. For the determination of the short range interaction force the influence of the long range force is removed by the method suggested by Guggisberg *et al.* [31]. In Figure 6.7(a) it can be observed that, while the tip approaches towards the sample surface, the attractive force between tip and hollow sites is increasing up to -0.28 nN. The center of the hollow site seems to be an area of constant attraction: F stays attractive within a dZ range of about 0.25 nm and a width of dX $\approx$ 2 nm. In contrast, the interaction force between tip and wire sites constantly remains more repulsive than that for the holes (F ≈ -0.12 to -0.15 nm) at their centers.

The extracted short range forces F_{short} shown in Fig. 6.7(b) show almost the same behavior than found in Figure 6.7(a). While the force between tip and hole sites is attractive up to $F_{short} \approx -0.1$ nN, the interaction between tip and wire sites becomes repulsive after 0.5 nm. By a closer approach of the tip towards the sample surface, the short range force becomes repulsive at $Z_{rel} \approx 0.15$ nm. A way to explain this behavior is, as already mentioned

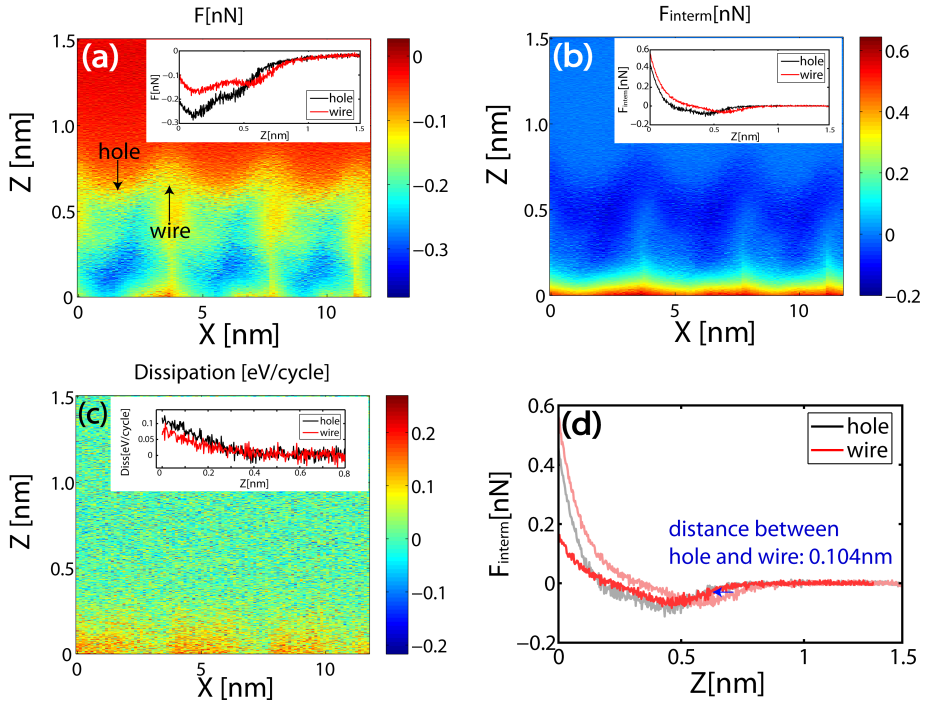

Figure 6.7: 2D spectroscopy data plots done above the *h*-BN/Rh(111) nanomesh: (a) Total force, (b) intermediate force (total force minus long-range force) and (c) dissipation. The insets of (a),(b) and (c) are site-dependent (hole, wire) 1D spectroscopy curves, extracted out of the 2D data. The inset curves are respectively averaged over 4 curves for each site. Parameters: f_{1st} =157 kHz, A_{1st} =10 nm, U_{Bias} =−500 mV.

before, to assume an elastic deformation of the wire sites. This idea is supported by the dissipation map in Figure 6.7(c). While at the hole sites the dissipation is constantly increasing up to ≈ 0.1 eV/cylce, at the wire site the dissipation is about 0.02 eV/cycle lower than on the hole site, being almost the same like the joule dissipative background. The latter arises due to the fact that the CPD compensation of the electrostatic force is done at only one single point above the surface not differing between the two different contrast sites. If the tip-sample distance is changed, the actual compensation voltage slightly differs from the CPD. Interestingly, if the wire sites are deforming, the according dissipation should increase due to an energy loss. However, if an elastic deformation is presumed this result is not striking. Because the dissipation is the average energy loss over one cantilever oscillation cycle, the energy loss by indenting the wire site by the

approaching tip is returned when the tip is retracted. Finally, in Fig. 6.7(d) the relative height difference between holes and wires is determined. The shift in z between the force-distance curves of the two sites is a measure for their height difference. Like that and also by extracting the heigth variation from Fig.6.6 a relative height of approximately $0.08 - 0.1$ nm is determined, which is with ≈ 0.05 nm almost double the value determined for example by STM [77].

6.2 KPFM

The advantage of KPFM compared to other methods like PES is the capability to resolute local variations in the contact potential (LCPD) of the tip-sample system on a small nanometer scale [96, 97, 98, 99]. The work function of layered materials like h-BN or graphene on Rh(111) or Ru(0001), which have differently bonded sites due to the formation of a superstructure, is varying with the distance of the 2D overlayer towards the substrate atoms [100]. Therefore, KPFM is a suitable method for the investigation of the properties of the 2D hexagonal superstructures presented in this thesis.
In Fig. 6.8 (a) and (b) the h-BN topography as well as the corresponding LCPD map are presented. Comparing Fig. 6.6 with the cross section of the topography (red line) in Fig. 6.8(c) as well as with the theoretical predicted structure [86, 87], it can be concluded, that the topography in Fig. 6.8(a) is inverted. Furthermore, the shape of the structure is slightly distorted, which can be explained by the influence of an asymmetric tip. From the LCPD map in Fig. 6.8(b) and the corresponding blue line in Fig. 6.8(c) the surface potential of the wire sites can be determined as $\approx -360 \pm 5$ mV and that of the hollow site as ≈ -375 mV ± 5. In former investigations by Chen *et al.* two electronic states for holes and wires were found: σ_α and σ_β [101]. This electronic structure corresponds to different local work functions which was revealed by PES on adsorbed Xenon atoms at hole and wire regions of the nanomesh [82]. There, a work function difference of 310 meV was measured, while we determined ≈ 15 mV. So, by Fig. 6.8(b) and (c) it can be identified that the the hollow sites, more strongly bond to the rhodium substrate, have a lower work function, while the weakly bonded wire sites seem to correspond to a relatively high work function.

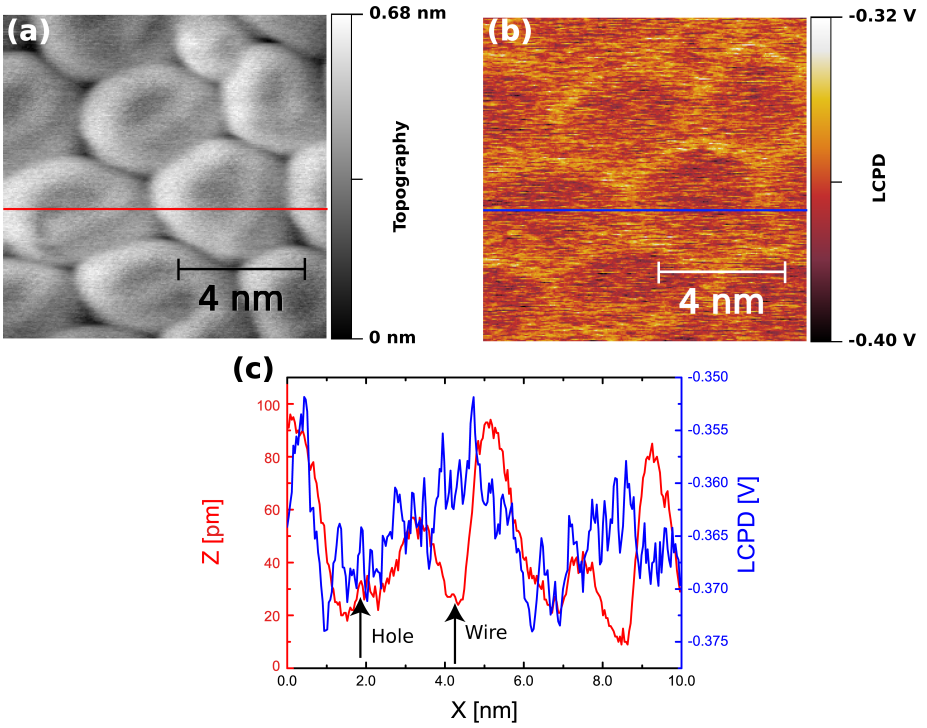

Figure 6.8: AM-KPFM measurement of h-BN on Rh(111) showing (a) an inverted topography and (b) the LCPD of the superstructure. (c) shows the cross sections made in (a) and (b). The holes are areas of lower workfuntion. $\Delta f = -8.5\,\mathrm{Hz}$, $A = 10\,\mathrm{nm}$, $U_{AC} = 500\,\mathrm{mV}$.

Figure 6.9 contains spectroscopy maps of the frequency shift and the LCPD versus the tip-sample distance. In the frequency shift map (left image) the transition of long- and short range regime of interactions between tip and the surface is evident, giving rise to two different contrasts. While at tip-sample separations down to 0.4 nm the long-range forces remain dominant, at smaller separations the short-range interaction regime is reached, leading to an inverted contrast in the topography. In Fig. 6.9(b) the simultaneously measured LCPD map with contour isolines of the frequency shift plotted into the same image, is shown. Comparing the deviation of the frequency shift and the LCPD map, a site dependend contact potential difference is observed. Far away from the surface, a LCPD of $-440 \pm 10\,\mathrm{mV}$ is found. Above the wire sites, this value increases to $-455 \pm 10\,\mathrm{mV}$ while for holes it even develops to $-470 \pm 10\,\mathrm{mV}$. Assuming that the inversion is caused

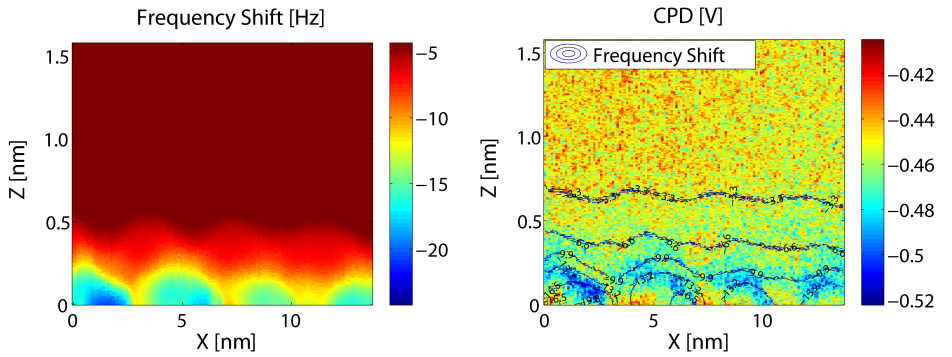

Figure 6.9: 2D AM-KPFM spectroscopy field for the *h*-BN layer: (a) Frequency shift map, (b)CPD map (sample is biased). Parameters: A = 10 nm, U_{AC} = 500 mV.

Site	Φ_{KPFM}	Φ_{PES}[15, 82]
(i) *above surface*	3.76 ± 0.01 eV	-
(ii) *wire*	3.75 ± 0.01 eV	≈ 4.49 eV*
(iii) *hole*	3.73 ± 0.01 eV	4.18 eV
(iv) *inverted wire*	3.77 ± 0.01 eV	-

Table 6.1: Comparison of the local work functions determined by the KPFM measurements (Fig. 6.9) with the results from PES experiments of [15, 82] with $\Phi_{\mathrm{Rh111}} = 5.52$ eV for the bare Rh(111) substrate [80] and a calibrated tip with $\Phi_{\mathrm{tip}} = 4.2 \pm 0.1$ eV. (* Using the result $\Delta\Phi_{hBN} \approx 310meV$ between hole and wire site from [82], whereas holes are areas of lower work function with $\Phi_{PES} \approx 4.18eV$ [15]).

by a deformation, meaning that the wires are indented and pressed towards the substrate surface due to a tip-sample interaction, in close proximity to the rhodium -435 ± 15 mV for the LCPD is found.

In table 6.1 these results are converted into work functions by the use of equation 3.31. The work function variation between holes and wires determined from the 2D KPFM spectroscopy measurement with ≈ 20 meV corresponds well with that one determined from Fig. 6.8. In contrast, by PES experiments a work function difference of 310 meV was stated [15, 82]. The discrepancy of the absolute values of the work function differences between PES and KPFM experiments, is explainable by the so-called averaging effect [102, 72, 103, 104, 105]. Due to the lateral interaction of the oscillating tip and cantilever with the long range electrostatic forces, so that the size of the cantilever contributes to the LCPD signal [106], the contact potential

difference is averaged. So, the difference between the two sites are detected to be smaller and the discrepancy to PES methods is reeasonable. Nevertheless, the local differences of the work function determined by KPFM are confirming other results of PES experiments that indentify the holes as areas of lower work function. The work function for the inverted wires $\Phi_{\mathrm{KPFM}} = 3.77 \pm 0.01\,\mathrm{eV}$ is increased compared to the normal ones due to the decreased distance between the nanomesh atoms and the Rh(111) surface at the wire areas after the inversion occured.

6.3 Summary

In this chapter, DFM measurements of the 2D hexagonal superstructure of *h*-BN on Rh(111), caused by a lattice mismatch of Rhodium and h-BN [77], have been presented. The structure can be divided into wire- and hole sites, whereas the holes are areas which are bonded to the Rh(111) substrate, while the wires are repulsed. During the preparation process of depositing borazine, the precursor for *h*-BN on Rh(111), small islands of *h*-BN are formed, which are growing together to complete a single monolayer. Like this, different translational domains are shaped [89] featuring a misalignment. The so caused stretching and skewing of the islands is leading to a variation in the mesh size and probably also to 4 different rotational domains, which were observed here. From the first high quality nc-AFM measurements ever performed on this nanomesh the periodicities of both the superstructure ($(2.8 \pm 0.4)\,\mathrm{nm}$) and the atomic lattice ($0.24 \pm 0.04\,\mathrm{nm}$) were determined, which are in agreement with the literature [14, 12, 82, 91, 75, 87, 92]. A contrast inversion was observed, at which the holes are imaged as elevations while the wires are depressed. A similar observation was made by STM, where a bias dependend contrast due to different states of different bonded sites was stated [14, 12]. On the other hand, the observed inversion could be brought into relation with small tip apex modifications as well as a tip-sample distance dependence. Latest seems to be connected with an elastic deformation of the wire sites. This assumption was investigated by multipassing measurements as well as 2D force spectroscopy maps, showing the evolution of the inversion. Additionally, out of the 2D spectras as well as the topography a determination of the height difference between the hole- and wire sites in nc-AFM was possible. The result of approximately

$0.08 - 0.1$ nm is with ≈ 0.05 nm almost double the value determined for example by STM [77]. Finally, KPFM measurements as well as 2D maps were in agreement with the results of former PES experiments [15, 82]. By both methods the holes were determined as an area of lower work function. The influence of the inversion on the work function was investigated. An indenting of the wire site leads to an increase of the work function, which probably can be explained by increasing the interaction of rhodium and *h*-BN states.

Chapter 7

Graphene on Ru(0001)

Carbon is one of the most frequently used basic materials on earth. It is the basis of all terrestric life and of humans technological improvements during all centuries. Under conditions which perfectly occur in red stars, it was originally formed by the fusion process of three helium or α-particles [107, 108]. Diamond and Graphite are the best known materials formed by pure carbon and are best examples that the way the carbon is arranged, strongly influences the mechanical and electronical material properties. More recently found carbon structures are fullerenes, nanotubes and graphene as the latest. Not only the Nobel Prize in physics of 2010 shows how big the scientific interest in these kind of material is. Extracted from the graphite bulk material by micromechanical cleavage [108], this twodimensional carbon structure has extraordinary characteristics like a linear band structure, giving electrons as massless Dirac fermions a bosonic behavior, an anomalous quantum Hall effect [5, 7], and a constant amplitude of the electron wave function in tunneling [109]. Interestingly, the rippling of graphene layers for example influences the electronic properties leading to decreased carrier mobility and many more [110, 111, 112]. Consequences of such rippling can perfectly be investigated on graphene superstructures grown on transition metals like ruthenium or rhodium.

Here, graphene on Ru(0001) is studied by means of Dynamic Force Microscopy and -Spectroscopy as well as Kelvin Probe Force Microscopy. This sample system is completely different from h-BN on Rh(111) but also forms a superstructure due to a mismatch between the overlayer- and substrate atoms. It was found, that analogue to the h-BN system, a

contrast inversion can occur that is also controllable by variations of the tip-sample distance. Twodimensional force spectroscopy fields verified this behaviour and it became apparent, that the change in contrast seems to be related to mechanical changes of the pattern, so that an elastic nature of the graphene superstructure can be estimated. Such a behaviour can open new possibilities for nano-mechanical devices like for example graphene based resonators or detectors [110, 111, 112, 113, 8].

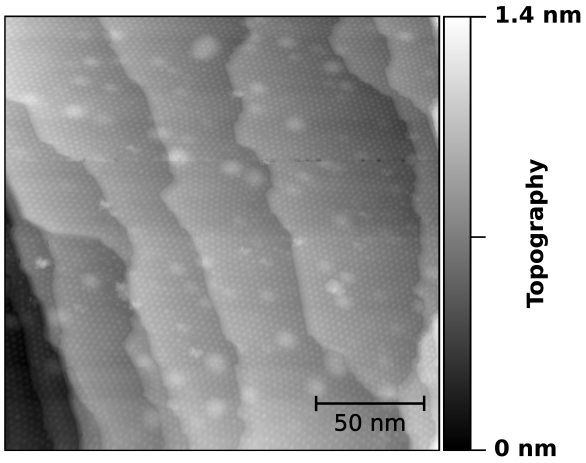

Figure 7.1: Overview of a grown monolayer of graphene on Ru(0001) with a regular superstructure. The big white spots, which are visible below the graphene are related to implanted impurities of argon in the ruthenium crystal due to the sputtering process. Scan parameters: $\Delta f = -10.4\,\mathrm{Hz}$, $A = 10\,\mathrm{nm}$, $U_{DC} = -908\,\mathrm{mV}$.

After the preparation process a sp^2-hybridized graphene monolayer is grown epitaxially on the Ru(0001) substrate as discussed in chapter 5.2.2. Figure 7.1 shows this regular graphene layer. As mentioned already for Fig. 5.3, the white spots appearing below the graphene layer are related to argon implantations due to the sputter cycles during the preparation process. Similar samples were already the subject of intense investigations in a series of studies performed by LEED, STM, ARUPS as well as by various theoretical techniques [76, 114, 115]. These studies concluded that the lattice mismatch between graphene and the ruthenium substrate leads to the formation of a hexagonal dislocation pattern. The unit cell of this superstructure consists of areas which are firmly attached to the substrate (so called *valley* sites)

and areas which appear partially detached from the substrate (*hill* sites) [116, 117].

The exact mismatch between C- and Ru-atoms was controversly discussed: More early investigations presented a model of matching (12×12) graphene unit cells matching to (11×11) atomic ruthenium unit cells [118]. This result was supplemented by LEED as well as STM experiments, modifying the model to (11×11) graphene unit cells sitting on (10×10) ruthenium cells [76]. Recent *Surface X-Ray Diffraction* (SXRD) experiments are predicting an even bigger cell size of (25×25) graphene cells matched on (23×23) ruthenium unit cells for the mismatch. [116, 119].

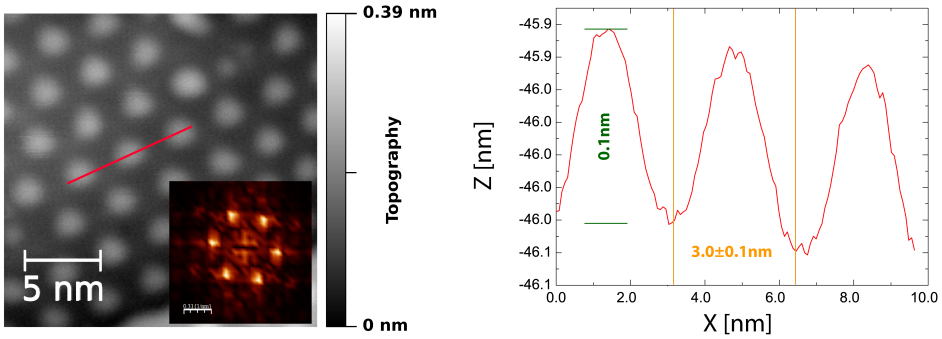

Figure 7.2: Image and cross section of the hexagonal graphene superstructure with a periodicity of 3.0 ± 0.1 nm and a corrugation height of ≈ 0.1 nm. Scan parameters: f_{1st} =171 kHz, A_{1st} =7 nm, Δf_{1st} =−8 Hz, U_{Bias} =−573 mV.

The non-contact atomic force microscopy measurement in Fig. 7.2 gives a closer look on the single layer graphene. The bright spots correspond to the ≈ 2 nm broad hills of the superstructure. Their periodicity, estimated from FFT filtering, is 3.0 ± 0.1 nm, which is in a good agreement to former investigations by STM and LEED that determined the hill site periodicity to ≈ 3 nm [114, 120, 121, 76, 118, 122]. The height of the graphene corrugation according to our AFM measurement was estimated to ≈ 0.1 nm, which is in good agreement with the former results. Experimental data done with SXRD as well as STM for example presented a height variation of $0.07 - 0.11$ nm between the hill- and valley sites [118, 116, 76]. In the STM case, this height was also found to be bias dependent [123, 76]. Furhtermore, in a theoretical work based on *Density functional theory* (DFT) calculations done by Stradi *et al.* [124] the corrugation height was calculated to about

0.12 nm. They pointed out the importance of van der Waals corrections for the DFT computing and could correct former results determining the corrugation height to ≈ 0.16 nm [117, 125, 100], so that experimental and theoretical values are now in good agreement.

Bimodal DFM Measurements

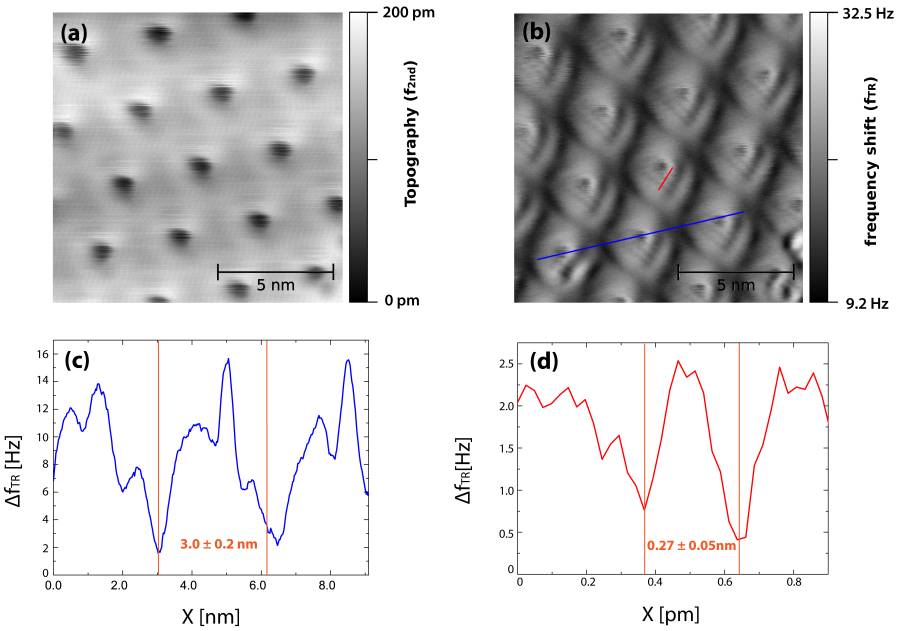

Figure 7.3: DFM images using the bimodal setup. (a) Topographic signal recorded by the use of the second cantilever resonance f_{2nd}. (b) Frequency shift Δf_{TR} of the simultanously recorded torsional mode. The blue and red lines are cross sections at which the red line corresponds to (c) showing the periodicity of the superstructure and the blue line to (d) with the corrugation of the carbon rings. Scan parameters: f_{2nd} =1.05 MHz, A_{2nd} ≈600 pm, Δf_{2nd} =−143 Hz, f_{TR} =1.5 MHz, A_{TR} ≈300 pm, U_{Bias} =−890 mV.

In chapter 3.3 bimodal DFM was introduced. As mentioned before, the advantage of this mode is the higher sensitivity towards short range forces and the low influence of long range forces due to the use of small cantilever amplitudes (<< 1 nm peak-to-peak). With the monomodal DFM mode, using only the first resonance, it was not possible to resolve single C-atoms or C-rings within the superstructure like it was possible for STM on graphene [126, 120, 76] or rather for the *h*-BN shown in the last chap-

ter. Thus, in Fig. 7.3 the results of bimodal DFM measurements above the graphene superstructure are shown. While the second flexural cantilever mode $f_{2nd} = 1.05\,\mathrm{MHz}$ was used for controlling the tip-sample distance (Fig. 7.3(a)), the torsional resonance frequency $f_{TR} = 1.5\,\mathrm{MHz}$ was excited by a second PLL, detecting the lateral force interaction by the frequency shift (Fig. 7.3(b)). Fig. 7.3(a) shows the topography channel using f_{2nd}. It can be seen, that the area, which should appear as hills are depressed. This observation can also be made in Fig. 7.3(b). There the superstructure is clearly visible and has got a triangular shape which is often observed in STM as well [114, 120, 118, 122, 76, 126]. Also, in the AFM measurement of Fig. 7.2 a slightly triangular shape of the superstructure pattern is visible. From the line profile in Fig. 7.3(c) the pattern periodicity is measured by FFT filtering to $3.0 \pm 0.2\,\mathrm{nm}$ similar to the measurements presented previously in this chapter. Additionally, the distance between twoatomic rows (lattice constant) can be estimated from a line profile (forward and backward channel) in Fig. 7.3(d) to $a \approx 0.27 \pm 0.05\,\mathrm{nm}$. The corresponding C-C interatomic distance is $a_{cc} = \frac{a}{\sqrt{3}} = 0.16\,\mathrm{nm}$. These values are in good agreement with the results of Vazquez de Parga *et al.* who determined an atomic lattice constant of $a \approx 0.246\,\mathrm{nm}$ [76]. Martoccia *et al.* [116], who showed a (25×25) superstructure, could reproduce the triangular structure of the hill areas by their calulations, which is in good agreement with the torsional measurements presented above. Additionally, they observed that a lateral motion of the graphene of up to $\approx 25 \pm 3\,\mathrm{pm}$ occurs which distorts the graphene bond length only slightly by 10 pm, so that a clockwise chiral structure is found. By this, they pointed out, that the largest motion of the graphene chirality happens at the flanks of the hills. Now, the results of the torsional measurement of Fig. 7.3(b) can be simplified by a direct comparison with their findings in [116]: The different strength of twisting probably leads to differences in the lateral forces of the graphene lattice, which can be visualized by the torsional mode. So, the flanks of the hills are causing a high torsional frequency shift, while the centers are imaged as darker areas, which is probably mainly influenced by the second flexural mode. Additionally and in accordance to [116], in Fig. 7.3(b) a chiral shape is visible at the flanks of the hill, which seems to verify the theoretical chirality calculated in [119].

7.1 Contrast Inversion

As already mentioned in the last chapter, it was demonstrated that during the scanning of the *h*-BN nanomesh a contrast inversion can occur. As explained, for the origin of this inversion the idea of an elastic deformation of the wire site on *h*-BN was pointed out, leaving the fundamental question, if that inversion can really be explained by a mechanical and topographical change of the structure due to the tip-sample interaction forces or not. If so, this contrast change has to occur also on different superstructured 2D layer materials like the here investigated graphene monolayer on ruthenium. On the other hand, in former STM and STS investigations, like in the boron nitride case, a controllable bias-related contrast inversion was observed [120, 114]. This was attributed to the different electronic states of graphene determined by the superstructure.

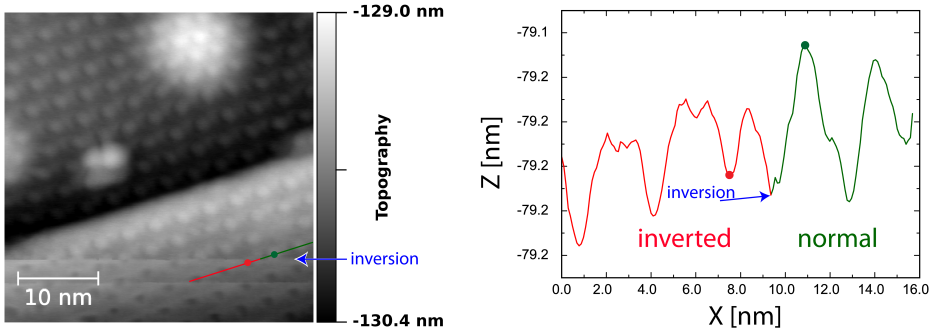

Figure 7.4: Accidentally occuring contrast inversion of the graphene superstructure on the ruthenium substrate. The former hills are changing to depressions in the lower part of the image corresponding to the inverted contrast. The contrast changes from one line to another (marked by blue arrow) like it could already be observed for *h*-BN, shown in the last chapter. The cross section is done across the inversion line. Its profile is shown on the right. The green part represents the "normal" hill-valley contrast and the red coloured part the inverted contrast with the hills changed to depressions. The dots are marking positions in the left image. Scan parameters: f_{1st} =172.8 kHz, A_{1st} =10 nm, Δf_{1st} =−8 Hz, U_{Bias} =−347 mV.

Figure 7.4 features an accidental inversion event of the graphene/Ru(0001) sample in DFM which is marked by a blue arrow. Obviously, in the topography signal, which is recorded from top to bottom, the contrast of the hill site changes from elevations to depressions. The cross section, done across

the line of inversion, leads to a deeper insight. The green part of the profile shown in the graph of Fig. 7.4 corresponds to the "normal" hill-valley contrast and the red part is correlated to the inverted contrast. The dots are marking the two extremas of the hill site. The profile points out that only the center part on top of the hill seems to be modified by the inversion while the areas left and right as well as the valley sites stay more or less constant. In the part of the line profile corresponding to the inverted contrast (red), a shoulder is visible just beside each depressed hill. So, it looks as if the center of the hills are simply flipped downwards by the tip-sample interaction.

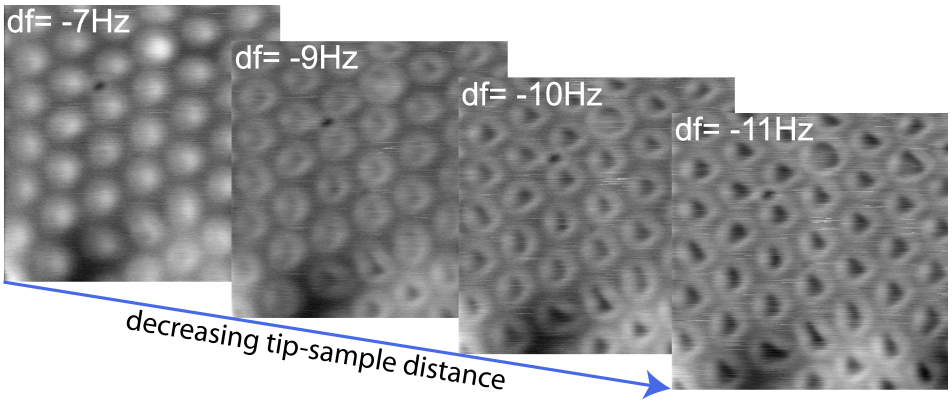

Figure 7.5: Four topographic images (20 nm×20 nm) recorded with the multipassing technique at different frequency shifts $\Delta f = -7$ Hz,-9 Hz,-10 Hz and -11 Hz respectively. For a continous compensation of the electrostatic force, KPFM was used. Parameters: A = 8 nm, $U_{CPD} = -487\text{to} - 537$ mV, $U_{AC} = 200$ mV.

Figure 7.5 shows four topographical images of the graphene layer acquired with the monomodal DFM mode and utilization of the Multipassing technique described in 4.5, making a direct comparison possible. The frequency setpoints of the frequency shift Δf are changing from -7 Hz to -11 Hz. Obviously, the superstructure is considerably modified by decreasing the tip-surface distance corresponding to an increasing frequency shift. The hill protrusions seem to be compressed by the tip so that in the end they appear as depressions (nanopits). Further details can be inferred from the cross sections in Fig. 7.6. Due to the characteristics of the force-distance curves, the four profiles normally are offset. Thus, for a direct comparison they had to be rearranged equivalent to chapter 6. From Fig. 7.4 it can be assumed, that the valley site stays constant during the inversion process. Hence, the

data points of the valley site of the four cross sections in Fig. 7.6(a) are fitted linear and adjusted to $z = 0$. The inner diameters of the formed nanopits when the tip is approached with a setpoint of $\Delta f = -11$ Hz is about 2 nm. With respect to the valley site, an upper limit for the total compression of the hills is given by approximately 120 pm.

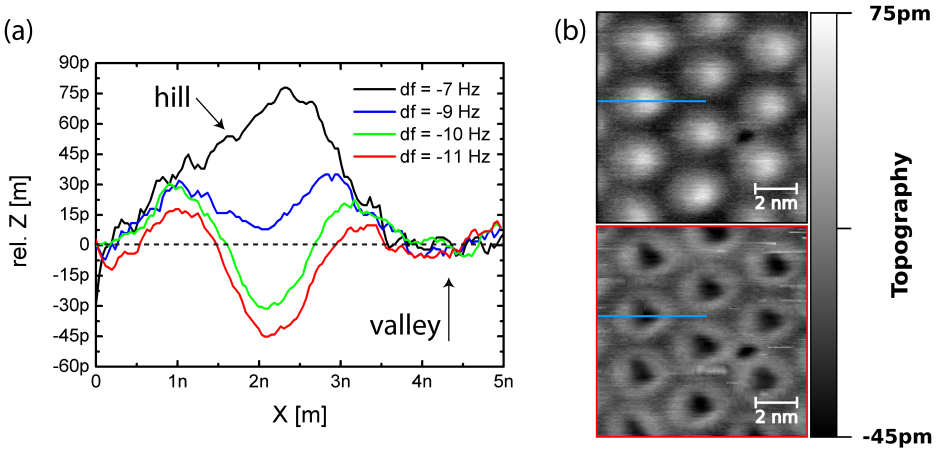

Figure 7.6: Detailed view of the contrast inversion recorded with the multipassing technique presented in Fig. 7.5 in chapter 4.5. The cross sections in (a) taken along the fast scan direction show the development of the hill and valley site marked by the blue lines in (b). The valley site of every curve is adjusted to $z = 0$ by linear fitting of the valley site and aligning the curve shapes. Therefore, with respect to the valley site, only the relative height variation of the hill site can be determined. The total change between normal ($\Delta f = -7$ Hz) and inverted contrast ($\Delta f = -11$ Hz) is ≈ 120 pm.

In Fig. 7.7 2D spectroscopy data is presented. Fig. 7.7(a) shows the total force F acting between tip and sample along a straight line crossing the centers of the hills. This force was calculated out of the Δf signal using the Sader-Jarvis method [36] described in chapter 3.2. The inset curves correspond to averaged values over three hill- (black) and valley- sites (red) in the presented force map. In the 2D data as well as in the red curve it is shown, that while the tip-sample force on the valley sites is continously increasing up to -0.5 nN, the hills (black curve) are behaving differently. After an increase up to -0.3 nN, the force F is again reduced on the top of them. A better insight can be gained by subtracting the long range van der Waals forces [31]. The resulting Fig. 7.7(b) represents in this case an "intermediate"

tip-surface force F_{interm} (again the inset curves in this figure are averaged). These forces are zero far away from the surface. When the tip approaches the surface on the top of a hill site, an attractive force F_{interm} turns up and reaches a maximum value of -0.15 nN at a tip-surface distance d ≈ 0.2 nm. After that, the attraction decreases till $\text{F}_{\text{interm}} \approx -0.08$ nN at the minimum distance which could be applied without crashing the tip (d ≈ 0.1 nm). On the valley sites, the attraction always increases up to -0.3 nN. These results strongly suggest that the graphene hills are elastically bent by the tip pressure.

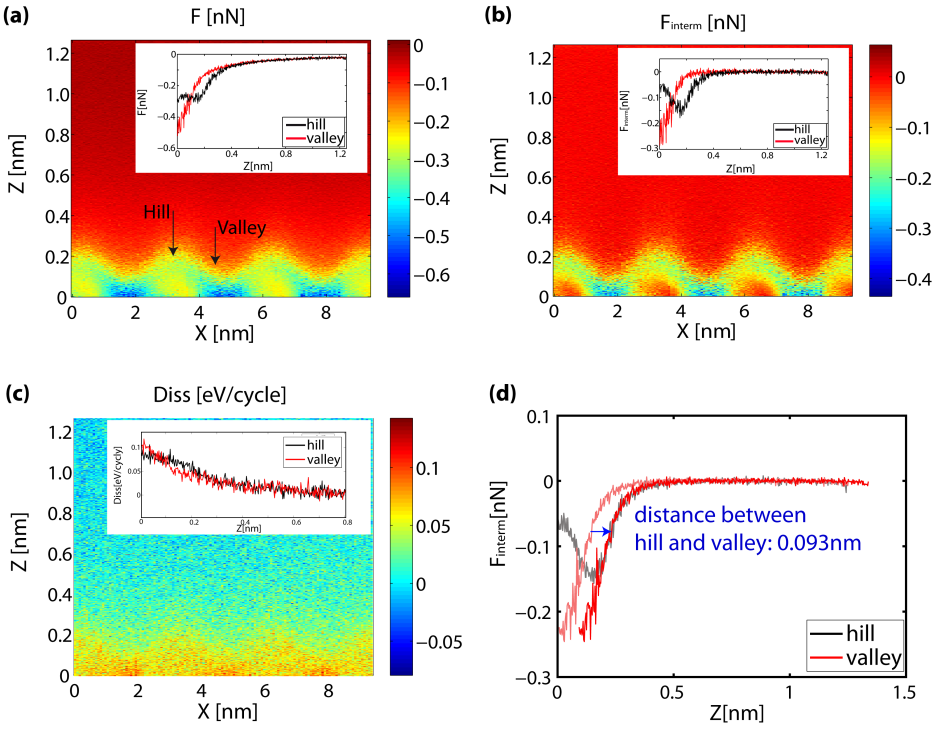

Figure 7.7: 2D spectroscopy data plots of the graphene/Ru(0001): (a) Total force, (b) intermediate force (total force minus long-range force) and (c) dissipation. The inset of (a),(b) and (c) are site-dependent (hill, valley) 1D spectroscopy curves, extracted from the 2D data. The curves are averaged over 4 single curves for every site. Parameters: A = 7 nm, $\text{U}_{\text{bias}} = -819$ mV.

A check of the dissipation signal in Fig. 7.7(c), which is also recorded during the spectroscopy, supports this assumption. Although, the dissipation signal shows a Joule dissipative behaviour, it can be seen, that the dissipation is increasing continously at the valley sites while it seems to sat-

urate on the hills, and keeps almost constant. This can be simply attributed to the fact that the energy spent to deform the elastic hills is returned to the tip within each oscillation cycle.
The spectroscopic data also enables for a more precise determination of the height difference between hill and valley due to the compensated drift by the AT function. Figure 7.7(d) shows the graphs of the intermediate force of (b) in more detail. The shift between hill and valley curve is equivalent to the height of the hills, so that with respect to the valley sites, the undeformed hills (black curve) show a height of about 93 pm, which is in good accordance to former experiments and calculations 80 ± 15 pm [118, 116].

7.2 KPFM

As for the h-BN nanomesh described in the last chapter, the determination of the work function is essential for the understanding of the structure. This material property is important in order to investigate and use the potential of graphene.
In Fig. 7.8 the topography- (a) and LCPD signal (b) of a KPFM measurement are presented. The signal-to-noise-ratio in Fig. 7.8(b) is typical for our experimental setup. Consistently with the measurements shown previously in this chapter, we find a periodicity of 3.4 nm. The LCPD signal presented in Fig. 7.8 (b) as well as in the cross section of (c) reveals contact potential variations of the superstructure of about -445 to -465 mV. It is noticeable that the LCPD maxima of the hills shown in (b) and (c) appear shifted and slightly smeared out compared to the graphene pattern in (a). By merging Fig. 7.8 (a) and (b) to (d) and in combination with (c) the lateral offset between the LCPD extremas and the graphene superstructure becomes obvious. The same behaviour was found in the backward signal as well (not shown here). Therefore, it is hardly possible to determine if the maximas in work function are corresponding to either hill or valley site of the graphene pattern. The origin of such a shift can for example be related to an asymmetric tip whereas one part is dominant for electrostatics while another one is mapping the topography. Nevertheless, it can be concluded that the determined difference in work function between hills and valleys is in the range of $\Delta\Phi = -20$ meV. This value is more than 10 times smaller than that determined by photon electron experiments [15] as well as DFT

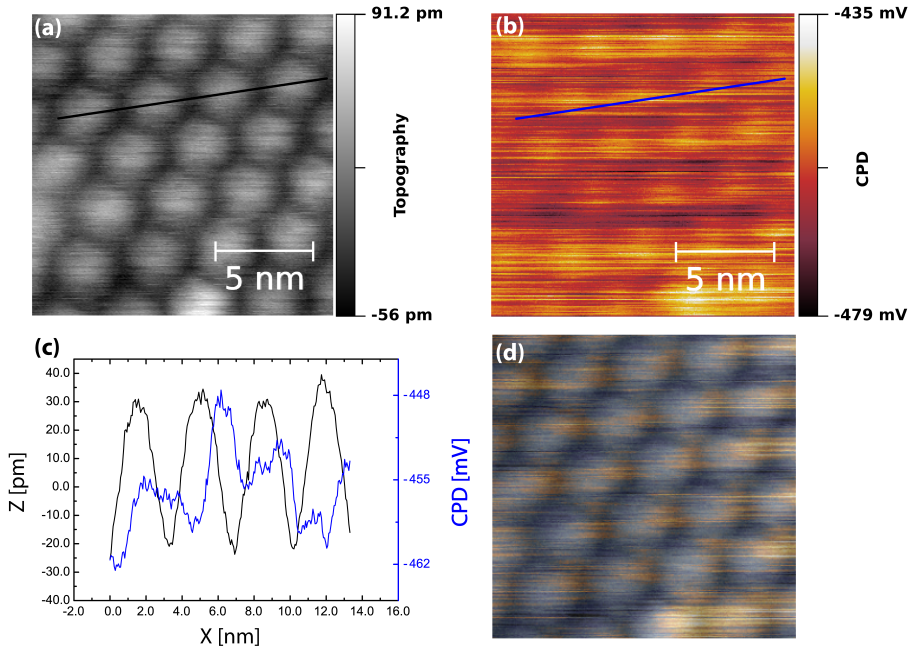

Figure 7.8: AM-KPFM measurement of graphene on Ru(0001) showing (a) te topography signal and (b) the LCPD of the superstructure. (c) shows the line profiles of the cross sections marked in (a) and (b). In (d) the images of (a) and (b) are merged for a better visualisation of the LCPD. $\Delta f = -37$ Hz, A = 10.4 nm, $U_{AC} = 500$ mV.

calculations [100], which is caused by the averaging effect in AM-KPFM as already discussed in case of the *h*-BN nanomesh in the KPFM section of chapter 6.

A better understanding of the site dependent LCPD of the graphene monolayer on Ru(0001) can be achieved from the twodimensional spectroscopy map presented in Fig. 7.9. In (a) a 2D map of the raw data of the frequency shift and in (b) a 2D LCPD map are shown. The contrast inversion, already described before, is clearly visible in the frequency shift. While it is first increasing continously above the valley sites, at a distance of 0.1 nm corresponding to ≈ -12.5 Hz the Δf signal turns and starts to become more repulsive than for the valley sites (< -15 Hz).
At a first glance a similar behaviour is observed in the LCPD map, in which also the corrugation corresponding to the graphene layer is visible. Towards the hills at Z $\approx$ 0.2 nm the LCPD signal increases to about -550 ± 10 mV but decreases again rapidly after Z $\approx$ 10 nm in vertical direction towards the

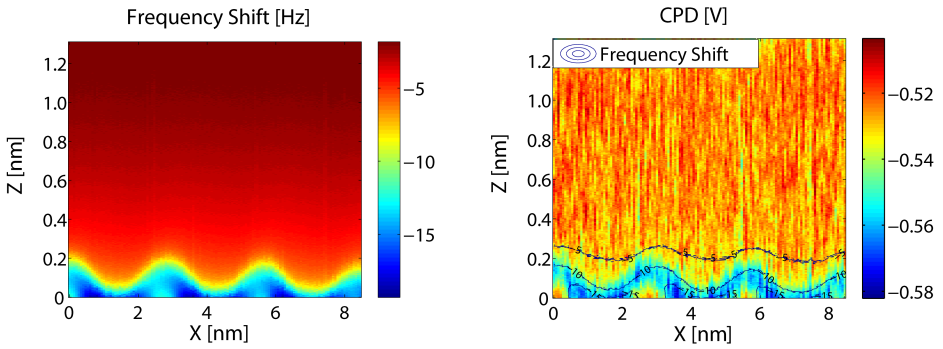

Figure 7.9: 2D spectroscopy map above the graphene layer: (a) Frequency shift map, (b) LCPD map by AM-KPFM. Parameters: A = 8 nm, U_{AC} = 100 mV.

surface to approximately -520 ± 10 V. Although the valleys LCPD jumps up to approx. -550 ± 12 mV at this site a continous increase of the contact potential with $U_{LCPD} \approx -570 \pm 12$ mV can be observed. On the one hand, this strongly reveals to two different work function values for the less bonded hills and the ruthenium strongly bonded valley sites and on the other hand, it shows a change in the work funtion which propably is coinciding with the contrast inversion observed in the topography.

Site	Φ_{KPFM}	Φ_{DFT}[100]
(i) *above surface*	3.68 ± 0.01 eV	3.77 eV
(ii) *hill*	3.64 ± 0.01 eV	3.72 eV
(iii) *valley*	3.62 ± 0.01 eV	3.52 eV
(iv) *inverted hills / close to ruthenium*	3.66 ± 0.01 eV	4.52 eV

Table 7.1: Comparison of work function results of the KPFM measurements (Fig. 7.9) with the results from DFT calculations presented in figure 2d of [100] using $\Phi_{Ru0001} = 5.52$ eV for bare Ru(0001) [80].

Assuming the same work function value for our n-doped silicon cantilever tip of $\Phi_{Tip} \approx 4.2 \pm 0.1$ eV done on graphite which is used in the last chapter 6, and a measured LCPD value for the hill site of $U_{hill} = 560 \pm 10$ mV, a work function of $\Phi_{hill} = 3.64 \pm 0.01$ eV can be determined out of equation 3.31. Doing the same for the valley site leads to a work function of $\Phi_{valley} = 3.62 \pm 0.01$ eV. In table 7.1 the values determined from the measurements are compared to the ones of the DFT calculations presented in figure 2d of [100]. As it can be seen, the values for the overall workfunction

for a monolayer graphene on Ru(0001) determined by the measurements and computations, are almost in the same range, whereas the experimental finding for the relative work function difference between hill and valley sites for example is ten times smaller ($\Delta\Phi_{\mathrm{KPFM}} \approx 20\,\mathrm{meV}$) than in the calculations ($\Delta\Phi_{\mathrm{DFT}} \approx 200\,\mathrm{meV}$). This is consistent with the result observed in Fig. 7.8 and can like in the case of *h*-BN be explained by the averaging effect of the cantilever as mentioned in the last chapter. Finally, it can be concluded that in the DFT calculations as well as in this KPFM measurements the hill sites occur as an area of higher work function compared to the valley sites with their π-bonding character. Some nanometers above the surface the work function is found to be bigger than directly at the hill and wire sites. The influence of the contrast inversion due to mechanical deformations of the hills is hardly comparable to other experiments done by PES or the referred calculations. Parallel to the ruthenium surface, between higher and lower C-atoms, the work function is computed by Wang *et al.* to be $\approx 0.7\,\mathrm{eV}$ higher compared to the substrate bound graphene at the valley site [100]. Therefore, an increase of the work function could be possible by a deformation. So the states of the hills are brought together with the ones from the ruthenium surface which could enable an higher interaction of the carbon atoms of the graphene with the ruthenium atoms. Unless calculations are done which are taking a possible deformation of the hill sites into account, for the moment it can only be referred to this KPFM measurements done in this work which show an increase of the hill site work funtion.

7.3 Summary

In chapter 7 a 2D hexagonal superstructure of graphene formed on Ru(0001) is investigated, prepared by CVD of ethylene on a Ru(0001) sample [123]. By performing high resolution DFM measurements the periodicity of the hill and valley site $3.0 \pm 0.1\,\mathrm{nm}$ was determined, being in accordance to former results of STM experiments [114, 120, 121, 76, 118, 122]. Using the bimodal DFM technique described in chapter 3.3 with the second vertical (tip-sample distance control) and the first torsional resonances, even the atomic lattice could be resolved showing a periodicity of a $\approx 0.27 \pm 0.05\,\mathrm{nm}$, equivalent to the results of Vazquez de Parga *et al.* [76]. Additionally, by this method, a clockwise chiral structure was observed, which was also

computed by MARTOCCIA *et al.* [116]. They stated, that the largest motion ($\approx 25 \pm 3$ pm) of the graphene chirality happens at the flanks of the hills. Probably, the different strength of twisting could lead to differences in the lateral forces of the graphene lattice. If so, they could be visualized by the torsional mode. Analogue to the *h*-BN case, a contrast inversion was shown, also observed in in STM experiments and explained by a controllable bias-relation [120, 114]. After the inversion process, the former elevations (hill site) are imaged as depressions, appearing lower than the valley sites. By multipassing scanning it was pointed out, that the hills are the only parts which are changing their corrugation to depressions (nanopits). Further investigations by 2D force spectroscopy figured out, that, as observed for the *h*-BN in the previous chapter, probably, an elastic deformation has to be taken into account. Additionally, the height variation determination between hill- and valley sites out of the force spectroscopy odata presented a value of 93 pm, which is in good accordance to former experiments and calculations 80 ± 15 pm [118, 116]. Finally spectrocopic maps as well as microscopic measurments with KPFM were done, pointing out the hills as areas of lower workfunction which was also observed before in calculations as well as PES experiments [100, 15]. The influence of the contrast inversion showed that the work function of the depressed hills becomes higher. If an indenting by the tip is assumed, this could be related to an overlap graphene and ruthenium states. Such a distance depence of the workfunction in graphene was already discussed before by WANG *et al.* [100].

Chapter 8

Comparative Conclusion and Outlook

This thesis is mainly focussed on dynamic force spectroscopy investigations of 2D hexagonal superstructures of h-BN and graphene on transition metals like Rh(111) and Ru(0001). Although both systems are different from the chemical and electrical point of view, they have a lot in common. Both, graphene as well as h-BN are shaping a sp^2-hybridized superstructure due to a lattice mismatch with their substrates. While the h-BN superstructure contains a repulsed, elevated wire site and surface bonded holes, the hill site of the graphene structure appears higher than the substrate bonded valley site. The single holes and hills have both a diameter of $\approx 2\,\mathrm{nm}$. Also their superstructure periodicity as well as atomic lattice constant are almost identical, which was shown here by the first high resolution monomodal and bimodal DFM measurements on these samples. From the electrical point of view both materials are dissimilar. In contrast to the graphene with its high conductivity, the h-BN is an insulator, which makes it an perfect counterpart of the graphene. On the basis of the partly similar and partly different properties of these materials, a comparative investigation by multiple DFM methods was done in this work. For both structures, a contrast inversion was observed and discussed. The repulsed and not substrate bonded sites, the hills in case of the graphene and the wires for the h-BN, showed a topographical switching, which could be controllably imaged. Furthermore, 2D spectroscopy measurements pointed out that the contrast inversion is probably related to a tip induced elastic deformation

of the hills or rather the wires. Additionally, 2D spectroscopy maps and topographic images with KFPM identified the holes of the *h*-BN and valleys of graphene as areas of lower work function which is due to their stronger interaction with the metallic substrate. These results verify former PES experiments by Brugger *et al.* as well as calculations done by Wang *et al.*. Futhermore, an influence of the inversion on the workfunction was found. By this, *h*-BN and graphene show the same behaviour. Assuming the elastic indention of the wire sites on the *h*-BN and the hill sites on the graphene respectively, seems to lead to such an increase of the work function, which is probably related by the overlap of metal- and overlayer states. In order to investigate the assumption of an elastic deformation of these superstructures more deeply, further experiments and theoretical calculations are needed. For example, friction or more precisely contact resonance measurements could be used to determine the stiffness of the elastic areas. If such a mechanical behaviour would be verified, this could be a great step for the development of for example new kinds of resonators or detectors.

Bibliography

[1] G. Binnig, C. F. Quate, and C. Gerber, Phys. Rev. Lett. **56**, 930 (1986).

[2] G. Binnig and H. Rohrer, Helv. Phys. Acta **55**, 726 (1982).

[3] D. M. Eigler and E. K. Schweizer, Nature **344**, 524 (1990).

[4] L. Gross, F. Mohn, N. Moll, P. Liljeroth, and G. Meyer, Science **325**, 1110 (2009).

[5] K. S. Novoselov, A. K. Geim, S. V. Morozov, D. Jiang, M. I. Katsnelson, I. V. Grigorieva, S. V. Dubonos, and A. A. Firsov, Nature **438**, 197 (2005).

[6] K. S. Novoselov, A. K. Geim, S. V. Morozov, D. Jiang, Y. Zhang, S. V. Dubonos, I. V. Grigorieva, and A. A. Firsov, Science **306**, 666 (2004).

[7] K. S. Novoselov, E. McCann, S. V. Morozov, V. I. Fal/'ko, M. I. Katsnelson, U. Zeitler, D. Jiang, F. Schedin, and A. K. Geim, Nat. Phys. **2**, 177 (2006).

[8] J. S. Bunch, A. M. van der Zande, S. S. Verbridge, I. W. Frank, D. M. Tanenbaum, J. M. Parpia, H. G. Craighead, and P. L. McEuen, Science **315**, 490 (2007).

[9] Y. Kawano and K. Ishibashi, Nat Photon **2**, 618 (2008).

[10] M. D. Stoller, S. Park, Y. Zhu, J. An, and R. S. Ruoff, Nano Lett. **8**, 3498 (2008), pMID: 18788793.

[11] J. Li and V. B. Shenoy, Appl. Phys. Lett. **98**, 013105 (2011).

[12] I. Brihuega, C. H. Michaelis, J. Zhang, S. Bose, V. Sessi, J. Honolka, M. Alexander Schneider, A. Enders, and K. Kern, Surf. Sci. **602**, L95 (2008).

[13] J. Zhang, V. Sessi, C. H. Michaelis, I. Brihuega, J. Honolka, K. Kern, R. Skomski, X. Chen, G. Rojas, and A. Enders, Phys. Rev. B **78**, 165430 (2008).

[14] S. Berner, M. Corso, R. Widmer, O. Groening, R. Laskowski, P. Blaha, K. Schwarz, A. Goriachko, H. Over, S. Gsell, M. Schreck, H. Sachdev, T. Greber, and J. Osterwalder, Angew. Chem., Int. Ed. Engl. **46**, 5115 (2007).

[15] T. Brugger, S. Günther, B. Wang, J. H. Dil, M. L. Bocquet, J. Osterwalder, J. Wintterlin, and T. Greber, Phys. Rev. B **79**, 045407+ (2009).

[16] K. Autumn, M. Sitti, Y. A. Liang, A. M. Peattie, W. R. Hansen, S. Sponberg, T. W. Kenny, R. Fearing, J. N. Israelachvili, and R. J. Full, Proceedings of the National Academy of Sciences **99**, 12252 (2002).

[17] J. E. Lennard-Jones, Proceedings of the Physical Society **43**, 461 (1931).

[18] J. N. Israelachvili, in *Intermolecular And Surface Forces*, 3rd edition ed., edited by Elsevier (Academic Press, Harcourt Brace Jovanovich, ADDRESS, 2011).

[19] H. Hamaker, Physica IV **10**, (1937).

[20] N. W. Ashcroft and D. N. Mermin, *Festkörperphysik*, 1 ed. (Oldenburg Wissenschaftsverlag GmbH, Toronto, 2005).

[21] P. M. Morse, Phys. Rev. **34**, 57 (1929).

[22] G. Binnig, H. Rohrer, C. Gerber, and E. Weibel, Appl. Phys. Lett.. **40**, 178 (1982).

[23] G. Meyer and N. M. Amer, Appl. Phys. Lett. **53**, 1045 (1988).

[24] K. Karrai and R. D. Grober, Appl. Phys. Lett. **66**, 1842 (1995).

[25] F. J. Giessibl, Appl. Phys. Lett. **73**, 3956 (1998).

[26] S. Torbrügge, O. Schaff, and J. Rychen, J. Vac. Sci. Techn. B **28**, C4E12 (2010).

[27] Y. Martin, C. C. Williams, and H. K. Wickramasinghe, J. Appl. Phys. **61**, 4723 (1987).

[28] T. R. Albrecht, P. Grütter, D. Horne, and D. Rugar, J. Appl.Phys. **69**, 668 (1991).

[29] F. J. Giessibl, Science **267**, 68 (1995).

[30] F. J. Giessibl, Phys. Rev. B **56**, 16010 (1997).

[31] M. Guggisberg, M. Bammerlin, C. Loppacher, O. Pfeiffer, A. Abdurixit, V. Barwich, R. Bennewitz, A. Baratoff, E. Meyer, and H.-J. Güntherodt, Phys. Rev. B **61**, 11151 (2000).

[32] U. Dürig, Surface and Interface Analysis **27**, 467 (1999).

[33] A. Baratoff and H. J. Hug, in *Noncontact Atomic Force Microscopy*, edited by S. Morita, R. Wiesendanger, and E. Meyer (Springer Verlag, Berlin / Heidelberg, 2002).

[34] W. Denk and D. W. Pohl, Appl. Phys. Lett. **59**, 2171 (1991).

[35] U. Dürig, Appl. Phys. Lett. **75**, 433 (1999).

[36] J. E. Sader and S. P. Jarvis, Appl. Phys. Lett. **84**, 1801 (2004).

[37] H. Hölscher, S. M. Langkat, A. Schwarz, and R. Wiesendanger, Appl. Phys. Lett. **81**, 4428 (2002).

[38] K. Ruschmeier and A. Schirmeisen, Phys. Rev. Lett. **101**, 156102 (2008).

[39] A. Schirmeisen, D. Weiner, and H. Fuchs, Phys. Rev. Lett. **97**, 136101 (2006).

[40] D. W. Pohl and R. Möller, Rev. Sci. Instrum. **59**, 840 (1988).

[41] M. Abe, Y. Sugimoto, O. Custance, and S. Morita, Nanotechnology **16**, 3029 (2005).

[42] S. Kawai, T. Glatzel, S. Koch, A. Baratoff, and E. Meyer, Phys. Rev. B **83**, 035421 (2011).

[43] S. Kawai, T. Glatzel, S. Koch, B. Such, and E. Baratoff, A. Meyer, Phys. Rev. B **81**, 085420 (2010).

[44] R. Bennewitz, A. Foster, L. Kantorovich, M. Bammerlin, C. Loppacher, S. Schär, M. Guggisberg, E. Meyer, and A. Shluger, Phys. Rev. B **62**, 2074 (2000).

[45] R. Pérez, I. Štich, M. C. Payne, and K. Terakura, Phys. Rev. B **58**, 10835 (1998).

[46] F. Giessibl, H. Bielefeldt, S. Hembacher, and J. Mannhart, Appl. Surf. Sci. **140**, 352 (1999).

[47] S. Kawai and H. Kawakatsu, Appl. Phys. Lett. **88**, 133103 (2006).

[48] S. Kawai, S. Kitamura, D. Kobayashi, S. Meguro, and H. Kawakatsu, Appl. Phys. Lett. **86**, 193107 (2005).

[49] S. Kawai, F. Rose, T. Ishii, and H. Kawakatsu, J. Appl. Phys. **99**, 104312 (2006).

[50] S. Kawai, T. Glatzel, S. Koch, B. Such, A. Baratoff, and E. Meyer, Phys. Rev. Lett. **103**, 220801 (2009).

[51] S. Kawai, T. Glatzel, S. Koch, B. Such, A. Baratoff, and E. Meyer, Phys. Rev. B **80**, 085422+ (2009).

[52] Y. Sugimoto, S. Innami, M. Abe, O. Custance, and S. Morita, Appl. Phys. Lett. **91**, 093120 (2007).

[53] J. Melcher, S. Hu, and A. Raman, Appl. Phys. Lett. **91**, 053101 (2007).

[54] S. Kawai, S. Kitamura, D. Kobayashi, and H. Kawakatsu, Appl. Phys. Lett. **87**, 173105 (2005).

[55] S. Kawai, N. Sasaki, and H. Kawakatsu, Phys. Rev. B **79**, 195412 (2009).

[56] O. Pfeiffer, R. Bennewitz, A. Baratoff, E. Meyer, and P. Grütter, Phys. Rev. B **65**, 161403 (2002).

[57] F. Giessibl, M. Herz, and J. Mannhart, Proc. Natl. Acad. Sci. U. S. A. **99**, 12006 (2002).

[58] M. Henzler and W. Göpel, *Oberflächenphysik des Festkörpers* (Teubner Studienbücher, Stuttgart, Germany, ADDRESS, 1994).

[59] S. W. Thomson (Lord Kelvin), Philosophical Magazine Series 5 **46**, 82 (1898).

[60] M. Nonnenmacher, M. O'Boyle, and H. K. Wickramasinghe, Appl. Phys. Lett. **58**, 2921 (1991).

[61] T. Glatzel, Lux-Steiner, E. Strassburg, A. Boag, and Y. Rosenwaks, *Scanning Probe Microscopy* (Springer Berlin / Heidelberg, ADDRESS, 2007), pp. 113–131.

[62] D. W. Abraham, C. Williams, J. Slinkman, and H. K. Wickramasinghe, J. Vac. Sci. Technol. B **9**, 703 (1991).

[63] S. Hudlet, M. Saint Jean, C. Guthmann, and J. Berger, The European Physical Journal B - Condensed Matter and Complex Systems **2**, 5 (1998), 10.1007/s100510050219.

[64] L. Nony, A. S. Foster, F. Bocquet, and C. Loppacher, Phys. Rev. Lett. **103**, 036802 (2009).

[65] F. Bocquet, L. Nony, and C. Loppacher, Phys. Rev. B **83**, 035411 (2011).

[66] A. Kikukawa, S. Hosaka, and R. Imura, Appl. Phys. Lett. **66**, 3510 (1995).

[67] S. Kitamura and M. Iwatsuki, Appl. Phys. Lett. **72**, 3154 (1998).

[68] S. Sadewasser, P. Jelinek, C.-K. Fang, O. Custance, Y. Yamada, Y. Sugimoto, M. Abe, and S. Morita, Phys. Rev. Lett. **103**, 266103 (2009).

[69] C. Sommerhalter, T. Glatzel, T. Matthes, A. Jäger-Waldau, and M. Lux-Steiner, Appl. Surf. Sci. **157**, 263 (2000).

[70] C. Gerthsen, in *Gerthsen Physik*, 21 ed., edited by D. Meschede (Springer Verlag, Berlin / Heidelberg, 2001).

[71] L. Howald, E. Meyer, R. Lüthi, H. Haefke, R. Overney, H. Rudin, and H. J. Güntherodt, Appl. Phys. Lett. **63**, 117 (1993).

[72] T. Glatzel, S. Sadewasser, and M. Lux-Steiner, Appl. Surf. Sci. **210**, 84 (2003).

[73] C. Sommerhalter, T. Matthes, T. Glatzel, A. Jäger-Waldau, and M. Lux-Steiner, Appl. Phys. Lett. **75**, 286 (1999).

[74] H. Diesinger, D. Deresmes, J.-P. Nys, and T. Melin, Ultramicroscopy **108**, 773 (2008).

[75] T. Greber, Cond. Mat. **1**, 54 (2009).

[76] A. L. Vazquez de Parga, F. Calleja, B. Borca, M. C. G. Passeggi, J. J. Hinarejos, F. Guinea, and R. Miranda, Phys. Rev. Lett. **100**, 056807 (2008).

[77] M. Corso, W. Auwarter, M. Muntwiler, A. Tamai, T. Greber, and J. Osterwalder, Science **303**, 217 (2004).

[78] E. Cavar, R. Westerstrom, A. Mikkelsen, E. Lundgren, A. Vinogradov, M. Ng, A. Preobrajenski, A. Zakharov, and N. Martensson, Surf. Sci. **602**, 1722 (2008).

[79] J. W. He and D. W. Goodman, Surf. Sci. **232**, 138 (1990).

[80] A. Nagashima, N. Tejima, Y. Gamou, T. Kawai, and C. Oshima, Phys. Rev. Lett. **75**, 3918 (1995).

[81] M. Paffett, R. Simonson, P. Papin, and R. Paine, Surf. Sci. **232**, 286 (1990).

[82] H. Dil, J. Lobo-Checa, R. Laskowski, P. Blaha, S. Berner, J. Osterwalder, and T. Greber, Science **319**, 1824 (2008).

[83] H. Karacuban, S. Koch, M. Fendrich, T. Wagner, and R. Möller, Nanotechnology **22**, 295305 (2011).

[84] B. Such, T. Trevethan, T. Glatzel, S. Kawai, L. Zimmerli, E. Meyer, A. L. Shluger, C. H. M. Amijs, P. de Mendoza, and A. M. Echavarren, ACS Nano **4**, 3429 (2010).

[85] O. Bunk, M. Corso, D. Martoccia, R. Herger, P. Willmott, B. Patterson, J. Osterwalder, J. Vanderveen, and T. Greber, Surf. Sci. **601**, L7 (2007).

[86] R. Laskowski and P. Blaha, J. Phys.: Cond.. Matter **20**, 064207 (2008).

[87] R. Laskowski, P. Blaha, T. Gallauner, and K. Schwarz, Phys. Rev. Lett. **98**, 106802+ (2007).

[88] M. Langer, Master's thesis, University of Basel, 2010.

[89] G. Dong, E. B. Fourré, F. C. Tabak, and J. W. M. Frenken, Phys. Rev. Lett. **104**, 096102+ (2010).

[90] I. Horcas, R. Fernandez, J. M. G. Rodriguez, J. Colchero, J. G. Herrero, and A. M. Baro, Rev. Sci. Instrum. **78**, 013705+ (2007).

[91] A. Goriachko, He, M. Knapp, H. Over, M. Corso, T. Brugger, S. Berner, J. Osterwalder, and T. Greber, Langmuir **23**, 2928 (2007).

[92] D. Martoccia, S. A. Pauli, T. Brugger, T. Greber, B. D. Patterson, and P. R. Willmott, Surf. Sci. **604**, L9 (2009).

[93] T. Arai and M. Tomitori, Appl. Surf. Sci. **157**, 207 (2000).

[94] S. Sadewasser and Th, Phys. Rev. Lett. **98**, 269701+ (2007).

[95] T. Shiota and K. Nakayama, Appl. Surf. Sci. **202**, 218 (2002).

[96] G. H. Enevoldsen, T. Glatzel, M. C. Christensen, J. V. Lauritsen, and F. Besenbacher, Phys. Rev. Lett. **100**, 236104+ (2008).

[97] T. Glatzel, L. Zimmerli, S. Koch, S. Kawai, and E. Meyer, Appl. Phys. Lett. **94**, 063303+ (2009).

[98] S. Kawai, T. Glatzel, H.-J. Hug, and E. Meyer, Nanotechnology **21**, 245704 (2010).

[99] S. Kitamura, K. Suzuki, and M. Iwatsuki, Appl. Surf. Sci. **140**, 265 (1999).

[100] B. Wang, S. GÃ$\frac{1}{4}$nther, J. Wintterlin, and M.-L. Bocquet, New J. Phys. **12**, 043041 (2010).

[101] W. Chen, K. P. Loh, M. Lin, R. Liu, and A. T. S. Wee, Phys. Stat. Sol. A **202**, 37 (2005).

[102] S. Sadewasser and M. Lux-Steiner, Phys. Rev. Lett. **91**, 266101 (2003).

[103] S. Sadewasser, P. Carl, T. Glatzel, and M. Lux-Steiner, Nanotechnology **15**, S14 (2004).

[104] F. Krok, K. Sajewicz, J. Konior, M. Goryl, P. Piatkowski, and M. Szymonski, Phys. Rev. B **77**, 235427 (2008).

[105] Y. Rosenwaks, R. Shikler, T. Glatzel, and S. Sadewasser, Phys. Rev. B **70**, 085320 (2004).

[106] G. Elias, T. Glatzel, E. Meyer, A. Schwarzman, A. Boag, and Y. Rosenwaks, Beilstein Journal of Nanotechnology **2**, 252 (2011).

[107] W. A. Fowler, Rev. Mod. Phys. **56**, 149 (1984).

[108] M. I. Katsnelson, Materials Today **10**, 20 (2007).

[109] M. I. Katsnelson, K. S. Novoselov, and A. K. Geim, Nat Phys **2**, 620 (2006).

[110] M. Katsnelson and A. Geim, Philosophical Transactions of the Royal Society A: Mathematical, Physical and Engineering Sciences **366**, 195 (2008).

[111] C. H. Lui, L. Liu, K. F. Mak, G. W. Flynn, and T. F. Heinz, Nature **462**, 339 (2009).

[112] L. Ju, B. Geng, J. Horng, C. Girit, M. Martin, Z. Hao, H. A. Bechtel, X. Liang, A. Zettl, Y. R. Shen, and F. Wang, Nat Nano **146**, (2011).

[113] D.-H. Kim and J. A. Rogers, ACS Nano **3**, 498 (2009).

[114] B. Borca, S. Barja, M. Garnica, J. J. Hinarejos, A. L. V. de Parga, R. Miranda, and F. Guinea, Semiconductor Science and Technology **25**, 034001 (2010).

[115] B. Borca, S. Barja, M. Garnica, D. Sánchez-Portal, V. M. Silkin, E. V. Chulkov, C. F. Hermanns, J. J. Hinarejos, A. L. Vázquez de Parga, A. Arnau, P. M. Echenique, and R. Miranda, Phys. Rev. Lett. **105**, 036804 (2010).

[116] D. Martoccia, M. Björck, C. M. Schlepütz, T. Brugger, S. A. Pauli, B. D. Patterson, T. Greber, and P. R. Willmott, New J. Phys. **12**, 043028 (2010).

[117] W. Moritz, B. Wang, M.-L. Bocquet, T. Brugger, T. Greber, J. Wintterlin, and S. Günther, Phys. Rev. Lett. **104**, 136102 (2010).

[118] S. Marchini, S. Günther, and J. Wintterlin, Phys. Rev. B **76**, 075429 (2007).

[119] D. Martoccia, P. R. Willmott, T. Brugger, M. Björck, S. Günther, C. M. Schlepütz, A. Cervellino, S. A. Pauli, B. D. Patterson, S. Marchini, J. Wintterlin, W. Moritz, and T. Greber, Phys. Rev. Lett. **101**, 126102 (2008).

[120] B. Borca, S. Barja, M. Garnica, M. Minniti, A. Politano, J. M. Rodriguez-Garcia, J. J. Hinarejos, D. Farias, A. L. V. de Parga, and R. Miranda, New J. Phys. **12**, 093018 (2010).

[121] B. Borca, F. Calleja, J. J. Hinarejos, A. L. V. de Parga, and R. Miranda, J. Phys.: Condens. Matter **21**, 134002 (2009).

[122] Y. Pan, H. Zhang, D. Shi, J. Sun, S. Du, F. Liu, and H.-j. Gao, Adv. Mat. **21**, 2777 (2009).

[123] A. L. V. Vázquez de Parga, F. Calleja, B. Borca, M. C. G. Passeggi, J. J. Hinarejos, F. Guinea, and R. Miranda, Phys. Rev. Lett. **101**, 099704 (2008).

[124] D. Stradi, S. Barja, C. Díaz, M. Garnica, B. Borca, J. J. Hinarejos, D. Sánchez-Portal, M. Alcamí, A. Arnau, A. L. Vázquez de Parga, R. Miranda, and F. Martín, Phys. Rev. Lett. **106**, 186102 (2011).

[125] B. Wang, M.-L. Bocquet, S. Günther, and J. Wintterlin, Phys. Rev. Lett. **101**, 099703 (2008).

[126] B. Wang, M.-L. Bocquet, S. Marchini, S. Gunther, and J. Wintterlin, Phys. Chem. Chem. Phys. **10**, 3530 (2008).

List of Figures

Acknowledgements

Until a PhD thesis is written it is a long and sometimes stony way. Also, one should never forget, that in order to be successfull, it is essential to learn from and work for a team. Therefore, I would like to thank Prof. Ernst Meyer, as the head of this team for his support during my thesis and his helpful advices as well as exhilarating discussion. Also, he broadened my scientific, cultural, and social horizon by giving me the possibility to attend conferences in several countries but also in switzerland, so that I could get into contact to some of the best scientists in our field. Next, many thanks also to Dr. Thilo Glatzel, who introduced me into the field of AFM and KPFM. Without his scientific knowledge, experience and dedication this group would not be as good as it is. Also, I learned from him, that in science a free mind for new ideas as well as patience but also hard work is fundamental. I do not want to miss the scientific but also private discussions we had. Also, I would like to thank Dr. Shigeki Kawai. I could benefit a lot from his endless technical and scientific know-how as well as his way to solve problems highly efficiently. Beside this, it was always a pleasure and fun to discuss, work or simply spend time with him. I also would like to acknowledge Dr. Bartosz Such who for me always was a kind of a stabilizing element within the group. His approaches to solve problems helped me a lot and he always reminded me, that there is also a life outside the university. He is missing in Basel. Also many thanks to Dr. Marcin Kisiel. Beside his outstanding fundamental knowledge in physics, the discussions with him were always filled with humour but also with good scientific ideas. I also want to thank Dr. Remy Pawlak who, as a very good young scientist, for me always was the bridge between PhD students and Post Doctoral researcher. I always enjoyed the time with him especially the discussions and jokes about french and german people. Many thanks also to Dr. Enrico Gnecco, not only because he was refery in my

thesis, but also because it is always a pleasure to be in contact with him. His ability to express and present scientific results by articles is exceptional and lead to many oustanding publications. The scientific database of our group is probably Prof. Alexis Baratoff. Although he increased the average duration of our group meetings, his tremendous experience is not abdicable for the group. I also like to acknowledge Dr. Pascal Steiner. Because of him we could enjoy free time as a group since he organized mainly our group excursions and activities, which I really miss. Additional thanks to Dr. Marco Wisse, Dr. Laurent Marot, and Alexander Bubendorf. Although we worked hardly together, the free time we had was always relaxing. It is a pitty, that the regular table has not established. I also would like to thank Roland Steiner for the deep and multifaceted discussions I could enjoy with him but also for his technical support. Whenever it was needed, he liked to help me. And ofcourse, I do not want to forget all my collegiate friends I have/had here in the group. As the oldest of them, I saw them in principal scientifically growing up. By this I like to mention Markus Langer, my first masters course student, Gregor Fessler (I still remember our first Grappa in Davos), Baran Eren and Matthias Wasem (there is still a paella missing) who all became good friends of me, which I do not want to miss. In the same way, I also like to acknowledge Christian Held, with whom I started my time in Basel and who became a very special and good friend of me. I also do not want to forget to thank Mrs. Weaver, Andreas Tonin, Christoph Werle (USA was a good time) and all other university staff members who are working everyday in the background for our scientific career. Many many thanks also to my beloved girlfriend Sweetlana, who always motivated, supported but also criticised me when it was needed for my thesis but also when other problems occured. Without her, it would have been much harder for me to be successfull. Last but not least, I would like to thank my parents. They are for me exceptional characters to which I owe everything I have in my life...

Curriculum Vitae

Personal Information

Sascha Koch
Georgstrasse 12
D-49326 Melle
Germany

EMail: Sascha.Koch@unibas.ch

Date of Birth: 14th of October 1981 in Glandorf, Germany
Nationality: German
Family Status: Unmarried

Career History

1993 - 2001	Secondary school: Gymnasium Melle in Melle, Lower Saxony, Germany
2001	Abitur (german university-entrance diploma)
2001 – 2002	Academic studies in the field of physics at the University of Münster, North Rhine Westfalia, Germany
2001	Change to the University Duisburg-Essen, Campus Duisburg, North Rhine Westfalia, Germany (former Gerhard Mercator Universiy of Duisburg)

2001 – 2002 continuance of the academic studies in physics at the University of Duisburg-Essen

10/2006 - 09/2007 **Diploma Thesis;** title: *Scanning Tunneling Microscopy of Organic Molecules – Investigation of PTCDA on insulating NaCl layers on a Cu(111)-substrate*

Diploma Exam Courses:
Solid State Physics
Thermodyn. & Relat. Electrodynamics
Surface Science & Scanning Probe Microscopy
Analytical Chemistry

01/2008 - 12/2011 **PhD Course** at the University of Basel, Department of Physics, in the group of Prof. Dr. Ernst Meyer. Topic: Noncontact Atomic Force Microscopy/Spectroscopy and Kelvin Probe Force Microscopy

PhD Thesis; title: *Investigation of hexagonal 2D super structures by dynamic force spectroscopy - Boron nitride and graphene on transition metals*

I am owing my university education to the following lecturers:
University Duisburg-Essen:
Prof. Dr. W. Kleemann, Prof. Dr. M. Schreckenberg, Prof. Dr. J. Bauer, Prof. Dr. D. Wolf, Prof. Dr. H.-J. Frohn (apl.), Prof. Dr. A. Lorke, Prof. Dr. P. Entel, Prof. Dr. H. M. Kuß (apl.), Prof. Dr. R. Möller
University Basel:
Prof. Dr. E. Meyer, Prof. Dr. M. Poggio, Dr. Th. Glatzel, Dr. E. Gnecco

Publication List

- S. Koch, D. Stradi, E. Gnecco, S. Barja, S. Kawai, C. Díaz, M. Alcamí, F. Martín, A. L. Vázquez de Parga, R. Miranda, Th. Glatzel, and E. Meyer
  Elastic Response of Graphene Nano-Domes
  (Submitted: June 2012)

- S. Koch, M. Langer, S. Kawai, E. Meyer, and Th. Glatzel
  Contrast Inversion of the h-BN Nanomesh Investigated by nc-AFM and Kelvin Probe Force Microscopy
  (Accepted in: Journal of Physics – Condensed Matter (April. 2012))

- H. Karacuban, S. Koch, M. Fendrich, Th. Wagner and R. Möller
  PTCDA on Cu(111) partially covered with NaCl
  Nanotechnology, 22, (29), (2011), 9

- S. Kawai, Th. Glatzel, S. Koch, A. Baratoff, and E. Meyer
  Interaction-induced atomic displacements revealed by drift-corrected dynamic force spectroscopy
  Phys. Rev. B, 83, (3), (2011), 035421

- S. Kawai, Th. Glatzel, S. Koch, B. Such, A. Baratoff, and E. Meyer
  Ultrasensitive detection of lateral atomic-scale interactions on graphite (0001) via bimodal dynamic force measurements
  Phys. Rev. B, 81, (8), (2010), 085420

- B. Such, Th. Glatzel, S. Kawai, S. Koch, and E. Meyer
  Three-dimensional force spectroscopy of KBr(001) by tuning fork-based cryogenic noncontact atomic force microscopy
  J. Vac. Sci. Technol. B, 28, (3), (2010), C4B1

- L. Gross, R. R. Schlittler, G. Meyer, L.-A. Fendt, F. Diederich, Th. Glatzel, S. Kawai, S. Koch, and E. Meyer
  Contacting self-ordered molecular wires by nanostencil lithography
  J. Vac. Sci. Technol. B, 28, (3), (2010), C4D34

- Th. Glatzel, L. Zimmerli, S. Koch, S. Kawai, E. Meyer
  Molecular assemblies grown between metallic contacts on insulating surfaces
  Appl. Phys. Lett., 94, (2009), 3

- T. Glatzel, L. Zimmerli, S. Koch, B. Such, S. Kawai and E. Meyer
  Determination of effective tip geometries in Kelvin probe force microscopy on thin insulating films on metals
  Nanotechnology, 20, (26), (2009), 264016

- S. Kawai, Th. Glatzel, S. Koch, B. Such, A. Baratoff, and E. Meyer
  Time-averaged cantilever deflection in dynamic force spectroscopy
  Phys. Rev. B, 80, (8), (2009), 085422

- S. Kawai, S. Maier, Th. Glatzel, S. Koch, B. Such, L. Zimmerli, L.-A. Fendt, F. Diederich, and E. Meyer
  Cutting and self-healing molecular wires studied by dynamic force microscopy
  Appl. Phys. Lett., 95, (2009), 103109.

- S. Kawai, Th. Glatzel, S. Koch, B. Such, A. Baratoff, and E. Meyer
  Systematic Achievement of Improved Atomic-Scale Contrast via Bimodal Dynamic Force Microscopy
  Phys. Rev. Lett., 103, (2009), 220801

Presentations

Oral Presentations

- Frontiers Bio-Nano Winter School, Workshop 2008, Zermatt, CH
- Deutsche Physikalische Gesellschaft (DPG) Frühjahrstagung 2008, Berlin, D
- Karlsruhe Institute of Technology (KIT) AFM-Workshop 2010, Karlsruhe, D
- DPG Frühjahrstagung 2010, Universität Regensburg, Regensburg, D
- NC-AFM 2010, International Conference on NC-AFM, Kanazawa, JAP
- Veeco 'Seeing at Nanoscale' Conference 2010, Basel, CH
- Materials Research Society Spring meeting 2011, San Francisco, USA
- Karlsruhe Institute of Technology (KIT) AFM-Workshop 2012, Karlsruhe, D
- Nanomanipulation Workshop 2012, Madrid, ESP

Poster Presentations

- NC-AFM 2008, International Conference on NC-AFM, Madrid, ESP
- National Center of Competence in Research (NCCR) Meeting 2008, Davos, CH
- NC-AFM 2009, International Conference on NC-AFM, Yale Univ., New Haven, USA
- NC-AFM 2011, International Conference on NC-AFM, Lindau am Bodensee, D